CRANFIELD UNIVERSITY

JUAN JOSÉ DE LA CUESTA TORRADO

EXPERIMENTAL ANALYSIS AND NUMERICAL OPTIMISATION OF THE EFFECT OF TRIGGER MECHANISM ON THE ENERGY ABSORPTION CAPABILITIES OF COMPOSITE TUBULAR STRUCTURES UNDER IMPACT LOADING

SCHOOL OF AEROSPACE, TRANSPORT AND MANUFACTURING
Advanced Lightweight Structures and Impact

MSc
Academic Year: 2017 - 2018

Supervisor: D Hessam Ghessamnejad
September, 2018

CRANFIELD UNIVERSITY

SCHOOL OF AEROSPACE, TRANSPORT AND MANUFACTURING
Advanced Lightweight Structures and Impact

MSc

Academic Year 2017 - 2018

JUAN JOSÉ DE LA CUESTA TORRADO

Experimental Analysis and Numerical Optimisation of the Effect of Trigger Mechanism on the Energy Absorption Capabilities of Composite Tubular Structures under Impact Loading.

Supervisor: D Hessam Ghesamnejad
September, 2018

This thesis is submitted in partial fulfilment of the requirements for the degree of MSc Advanced Lightweight Structures and Impact

ABSTRACT

This Thesis was conducted in collaboration with the Cranfield Impact Centre. The main aim of the project was to perform an experimental characterisation of how different trigger mechanisms affect the performance of composite tubular energy absorbers and use the results to create and validate an FEA model in order to develop a triggers' redesign.

CFRP tubular samples were manufactured through a hand lay-up process. Three tubes were produced to test bevel triggers at 30º and 60º as well as a tulip trigger with 4 tips at 60º. Samples were tested in a drop tower rig with a mass of 80 kg at 5 m/s. Experimental results proved that 30º chamfer produced higher SAE and lower peak force than chamfer at 60º. Tulip type specimen presented lower SAE results than bevel type but a smooth force response interesting for crashworthiness purposes.

A numerical model was created using LS-Dyna. The model was used to explore further the experimentally studied triggers. Bevel triggers at 15º, 30º, 45º and 60º were compared as well as 4 and 6 tips tulips at 60º and 90º. In overall, chamfer tubes performed better in all cases than the tulip tubes. Within these, chamfer at 45º presented the best results with a SAE of 43.6 kJ/kg. Regarding the tulip triggers, it was proved that increasing the tips' angle is more effective than increasing the number of tips, however it can produce instabilities in the triggers' crushing. By contrast, tulip models with a higher number of tips showed more stable crushing behaviours. Combining both benefits, the tulip geometry with 6 tips at 90º exhibited the best results for this trigger, with a SAE of 39.4 kJ/kg improving the experimental baseline an 8.8%.

Keywords:

Crashworthiness, Finite element modelling, Testing, Progressive failure, Optimisation, Automotive

TABLE OF CONTENTS

LIST OF FIGURES

LIST OF TABLES

LIST OF EQUATIONS

LIST OF ABBREVIATIONS

CFE	Crushing Force Efficiency
CFRP	Carbon Fibre Reinforced Polymer
CIC	Cranfield Impact Centre
EA	Energy Absorption
FEA	Finite Element Analysis
FEM	Finite Element Method
FIA	*Federation Internationale de l'Automobile* (International Automotive Federation)
HIC	Head Injury Criterion
ID	Inner Diameter
ILS	Interlaminar Shear Strength
OD	Outer Diameter
SAE	Specific Absorbed Energy
SE	Stroke efficiency
UD	Unidirectional

1 INTRODUCTION

1.1 Motivation

The increase in the use of transportation systems produced in the second half of the XX Century led to a demand on the enhancement of the vehicles for the passenger safety [1]. In the automotive sector, the number of regulations and actions taken to improve the roads and vehicles safety has been increasingly growing since then [2]. Recently, the United Nations declared the 2011-2020 time period as the Decade of Action for Road Safety, aiming the reduction of fatalities related to automotive incidents by means of improving the safety of both the roads and vehicles [3]. These facts depict the importance that crashworthiness has got in the recent years.

The crashworthiness of a structure or subcomponent is related to its crash resistance and involves its energy absorption capabilities during an impact scenario. Normally, this impact's kinetic energy is absorbed plastically by crash components which are designed for this purpose. This energy absorption, as explained later in section 1.2, is produced by means of both the device's collapsing force and deformation. Therefore, the control of the accelerations transmitted to the vehicle's occupants (related with the crushing forces) as well as the component's deformation which must ensure a survivability area for the passengers are key [4].

Crashworthiness has been considered in vehicle design since 1952 when Bela Barényi patented a distributed strength vehicle's body concept, shown in Figure 1-1 [2]. Since then, in order to achieve this car body crashworthy design, several solutions as plastic collapse struts, energy absorbing frames, crumple zones and bumpers as well as the occupants' compartment and the crash cushion designs have been introduced. Plastic collapse struts or tubes involve a convenient solution since they represent not only crash devices but also structural components driving this to weight savings [4].

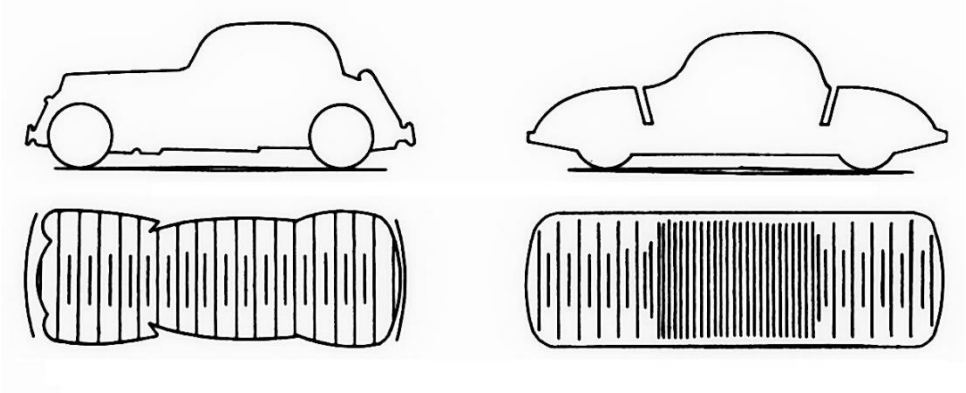

Figure 1-1. Bela Barényi patented concept considering car's body safety. (Adapted from Seiffert [2]**).**

The introduction of composite materials in the automotive sector was produced in the 1980s driven by their proven benefits shown in Formula One applications [4]. These benefits rely on their high strength and low density which leads to high values of specific strength and stiffness [5]. This produces a considerable weight reduction which makes these materials very suitable for facing some of the challenges in the transportation sector nowadays [5–8]. Despite being impact damage one of the main drawbacks when considering composites for structural applications [9] their engineered design has been proven to be able to meet not only the highest stiffness, strength and weight requirements but also the crashworthiness ones in a demanding sector such as Formula One [10]. In the case of crashworthy tubular components, in fact, they have been proved to provide better results than equivalent metallic solutions [4].

1.2 Theoretical Background

As introduced previously, crashworthiness is related with the capability of a structure or subcomponent to absorb the energy during an impact scenario. The energy driving the impact is the kinetic energy of the impactor, as represented by Equation (1-1). Normally, this energy will be absorbed by the crashworthy components by means of their controlled failure. Definition of failure can be different depending on the component's application [4]. In the case of crashworthy elements, their desired performance is that of failing to absorb impact energy thus preventing structural damage and occupant's injuries.

Therefore, in some applications, a certain and proper failure mode is a design requirement and not a design constraint.

$$E_K = \frac{1}{2}mv^2 \quad \textbf{(1-1)}$$

Where *m* represents the impactor's mass and *v* its velocity.

As said before, impact energy should be absorbed by means of the component's internal energy or work. As presented in Equation (1-2) [11], this figure depends on the failure load and crushing distance or displacement. If the force-displacement response during a crushing process is plotted, the absorbed energy represents the area under the curve.

$$W = \int FdS \quad \textbf{(1-2)}$$

Where *F* represents the load carried by the crushing device and *S* represents the displacement produce in the component during the impact under the certain load.

Comparison between progressive failure and the common sudden failure, characteristic of other structural components, is described in Figure 1-2 and Figure 1-3. Moreover, Figure 1-3 depicts the suitability of progressive failure for energy absorption purposes due to the increase of area under the force-displacement curve. To reach this particular collapsing mode, failure initiators or *triggers* are required [12]. These will prevent the sudden global failure of the structure by creating stress concentrators that will promote the collapse of the component in a stable manner [13].

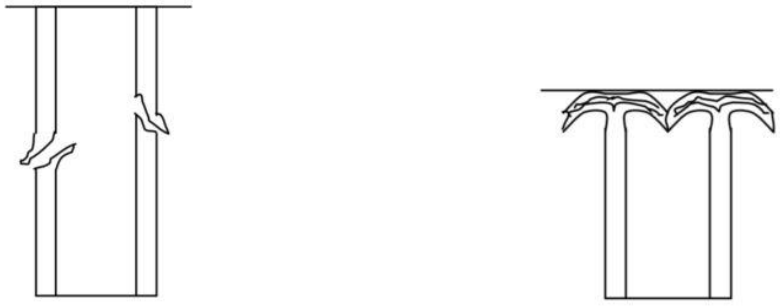

a) b)

Figure 1-2. Comparison between catastrophic failure behaviour, a), and progressive failure behaviour, b). (Adapted from Rabiee [11]**).**

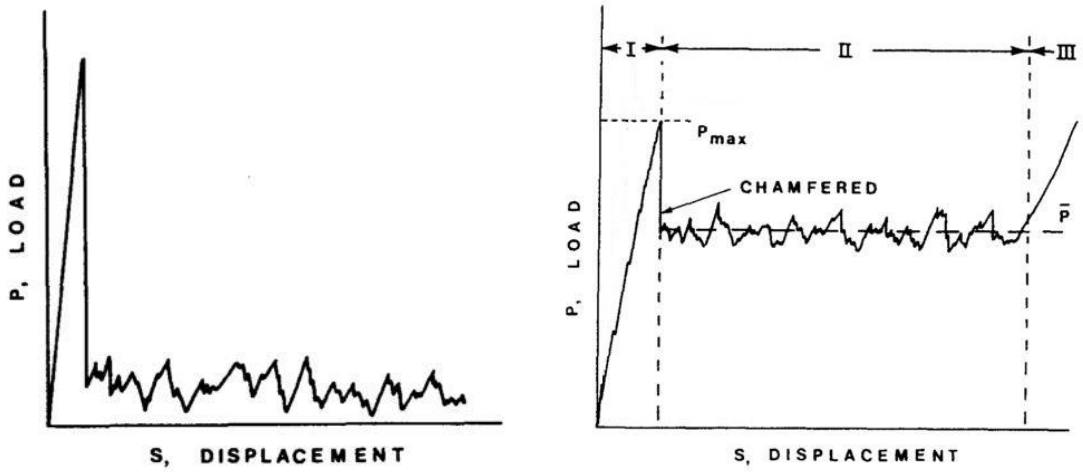

a) b)

Figure 1-3. Examples of the force-displacement response of catastrophic, (a), and progressive, (b), collapsing failures. (Adapted from Hull [12]**).**

Three main phases are identified within the progressive collapse of components in Figure 1-3 (b). Phase I represents the loading stage, the load rises elastically until reaching the material limit triggered by the failure initiator, F_{max}. Phase II represents the progressive failure itself and is driven by the crushing force. Finally, as shown in phase III, a bottoming out can take place, where the load increases again rapidly due to a compaction of the remaining material after failure [4,12].

The two main parameters of progressive failure are the crushing load and distance. These two are combined (trough Equation (1-2)) to meet the energy absorption requirements. Therefore, the crashworthy component will either carry high forces through a short deformation or lower forces through a large deformation [4]. Within these two, forces are critical for the occupant's safety, since these will drive the accelerations transmitted from the impactor to the passengers through the crashworthiness device. These accelerations are the responsible of the possible passengers' injuries and fatalities [14], and their threshold or safe limits are normally assessed by means of the HIC parameter or the Eiband's curve [15]. Regarding the deformation occurring during the impact, this one must ensure that all the energy is absorbed in the crashworthy component's length, thus not transmitting energy to the passengers' space. Both the initial peak force, which will be short in time but large in magnitude, or the crushing sustained load which normally will be smaller than the triggering force but sustained during a longer time period, should be taken into account for occupant's safety assessing. These may cause a cabin deformation that would threaten the occupants' survivability area enlarging the amount and severity of secondary impacts and passengers' injuries [14].

1.2.1 Crashworthiness Performance Parameters

Several parameters can be used to assess the crashworthiness performance of energy absorption components. These values are based on the force-displacement response which represents the crushing behaviour of the components. The main parameters used are [6,16,17]:

- Peak force (F_{max}): maximum load value in the force-displacement curve.
- Energy absorption (EA): area under the force-displacement curve, as shown in Equation (1-3).

$$EA = \int_0^{\delta_f} F d\delta \tag{1-3}$$

Where F is the force carried by the component, δ its deformation and δ_f the final crushed distance.

- Displacement or crushing (d): the amount of crushing distance or impactor's axial displacement during the impact.
- Mean force (F_m): calculated as the absorbed energy over the components maximum deformation, as included in Equation (1-4). Simplifies the force-displacement response assuming a constant load crushing behaviour.

$$F_m = \frac{EA}{\delta_f} \quad \textbf{(1-4)}$$

- Specific Energy Absorption (SAE): represents the absorbed energy over the mass of the crushed component. Very helpful when tubes of different configurations and materials are studied and compared. Its calculation is shown in Equation (1-5).

$$SAE = \frac{EA}{A_s \cdot \rho \cdot \delta_f} \quad \textbf{(1-5)}$$

Where A_s represents the specimens' cross-section and ρ its density.

- Crushing Force Efficiency (CFE): calculated as the ratio between mean and peak force (Equation (1-6)).

$$CFE = \frac{F_m}{F_{max}} \quad \textbf{(1-6)}$$

- Stroke efficiency or use ratio (SE): it's the ratio of the crushed distance over the component's initial length, as shown in Equation (1-7).

$$SE = \frac{\delta_f}{L_0} \quad \textbf{(1-7)}$$

Where L_0 represents the initial length of the crashworthy component.

1.3 Objectives

- Getting an understanding of the crashworthiness behaviour of the axial crushing of composite tubular structures.
- Reviewing the effect of trigger mechanism on composite energy absorbers.
- Reviewing the FEM techniques reported in the literature that are used to simulate the performance of axial crushing structural components.
- Performing an experimental comparison among 3 different trigger mechanisms.
- Creating an FEA dynamic model and using experimental results to validate it.
- Performing a design optimisation of the trigger mechanisms by means of the validated FEA model.

2 LITERATURE REVIEW

This section aims to give an overview of the use and simulation techniques of composite tubular structures for crashworthiness purposes. Research on these topics was carried out both to get a better understanding of this technology and to set a baseline for present work, which aimed to find improvements in this area.

2.1 Crashworthiness of Tubular Energy Absorbers

The crashworthiness behaviour of tubular structural components is based on their progressive failure to achieve large amounts of absorbed energy. Comparison between progressive failure and the common sudden failure, has been already described in section 1.2.

Regarding the progressive failure behaviours of tubular components, axial crushing and plastic folding are the ones taking place [12]. Plastic folding of the tube's skin (Figure 2-1, a)) is characteristic of metallic structures [11]. The design and performance of these metallic crashworthy components are well-known and has been extensively studied by several authors [1,18–21]. On the other hand, axial crushing (Figure 2-1, b)), takes place in composite components [4] which normally do not show this local buckling response as metallic structures do [12]. Among these main two failure modes, the progressive axial crushing of composite components has been proved to yield to higher values of absorbed energy [4,12,22,23]. This improved crashworthiness, in addition to the weight reduction that they produce due to their higher specific strength which involves economic and environmental benefits [22], make composite energy absorbers to be the ones under the spotlight nowadays.

However, the complex failure mechanisms taking place within their collapse (described in section 2.2) and the amount and interaction of parameters affecting the behaviour of these light-weight components (included in section 2.3) represent a great challenge when they are the object of design and optimisation [22]. This is precisely where the interest of this work relied, on enlarging the knowledge in one of these features such as the trigger mechanisms.

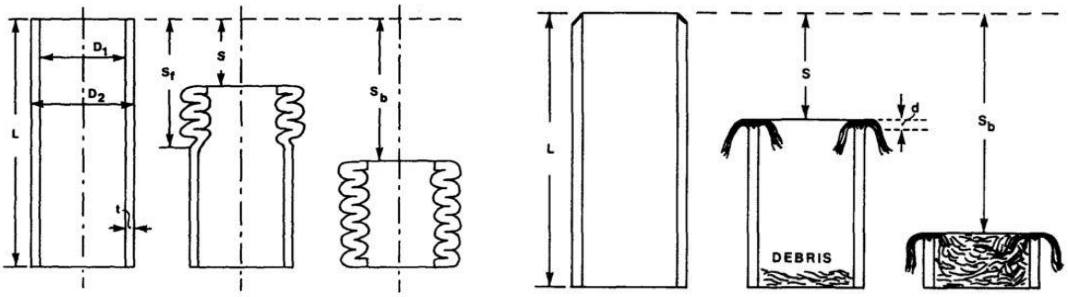

a) b)

Figure 2-1. Progressive plastic folding, (a), and progressive axial crushing, (b), comparison. (Source: Hull [12]**).**

2.2 Axial Crushing of Composite Tubes under Axial Crushing

As said before, the current trend points towards composite tubular structures as crashworthy solutions not only in the automotive industry but also in the aerospace one [4,13,22]. Therefore, it is necessary to describe in detail the behaviour and parameters affecting the axial crushing of these components which, as justified previously, are the most convenient solutions for energy absorption purposes.

Different collapsing modes can take place within the stable axial crushing of composite components. Several authors such as Farley [24] and Hull [12] identified three main crushing modes: transverse shear or fragmentation, lamina bending or splaying and local buckling. Folding or local buckling takes place mainly in ductile composites such as aramid [4,25] but can appear also in carbon composites under certain conditions as shown by Hosseini [6] and stated by Mamalis [4]. Transverse shear and lamina bending are the characteristic mechanisms of high stiffness components [24] and therefore of the CFRP energy absorbers which are the object of this work. Figure 2-2 shows this two main mechanisms as well as the brittle fracture which is a combination of them two [24]. The likelihood to occur for each of them will be strongly dependent on material properties, layup configuration, specimen geometry and loading conditions [11,24].

Other unstable mechanisms such as global buckling, barrel or interpenetration can take place [6] and should be avoided due to their low energy absorption capabilities.

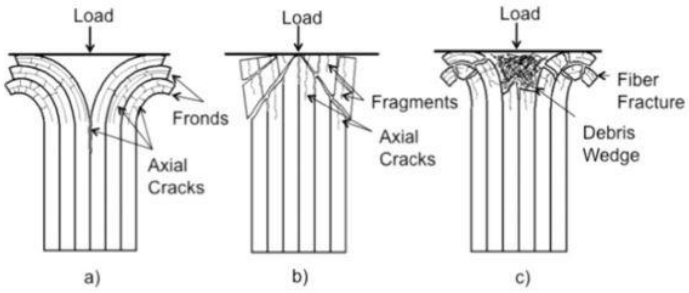

Figure 2-2. Possible axial crushing modes. Lamina bending/Splaying (a), fragmentation/transverse shear (b) and brittle fracture (c). (Source Hosseini [6]**).**

Several and complex failure mechanisms take place within the lamina bending and transverse shear mechanisms. Transverse shear involves the appearing of interlaminar cracks under Modes I and II, and longitudinal intralaminar cracks with a length which is shorter than the laminate thickness. This produces the fracture of the lamina bundles that are formed by the progression of the interlaminar cracks. Energy during this scenario is carried by this breaking phenomenon and the cracks initiation [24]. The process is illustrated in Figure 2-3.

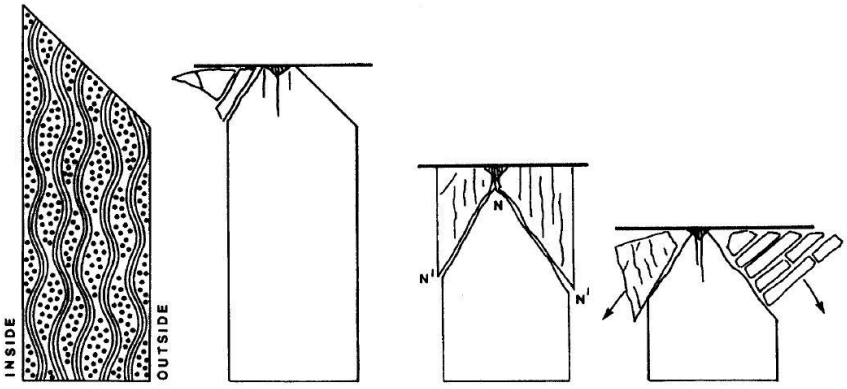

Figure 2-3. Transverse shear/Fragmentation failure process. (Source: Hull [12]**).**

On the other hand, in lamina bending, these fronds and debris of material failed during the process initiation are sustained during the crushing. This laminate debris act as a wedge aiding in the mode I opening of the central crack. This process (illustrated in Figure 2-4) is sometimes described as petal formation.

Within this mechanism, the energy is not absorbed by the laminate fracture anymore but by the mode I interlaminar shear of the splaying laminate, the mode II interlaminar shear between the plies at the fronds, the bending resistance of the laminas and friction between the fronds against the impactor surface and between the laminate wedge and the fronds [12,24]. As observed, this mechanism is much complex than the fragmentation mode since involves a larger amount of micro-mechanic failure processes.

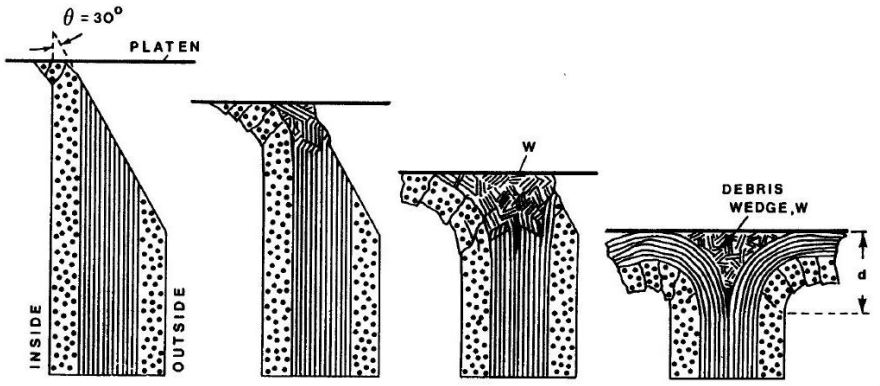

Figure 2-4. Lamina bending/fibre splaying failure process. (Source: Hull [12]**).**

As said before, brittle fracture appears as a combination of these two crushing modes. On it, the fronds are sustained until they fail by either tensile failure, compression/shear, buckling or interlaminar shear (represented in Figure 2-5). The feature making one of these two crushing modes to occur or driving the degree of interaction among them in the brittle fracture mode is the level of lateral support produced by the amount and position of the hoop fibres within the laminate [12]. High ratios of the hoop to axial fibres will produce failures closer to transverse shear and, contrarily, lower values of this ratio will produce the typical large petals of the lamina bending. This process encompasses all the failure mechanisms included in both the fragmentation and the lamina bending mode. Therefore, appears to be the desired crushing mechanism in the components' design since yields to higher energy absorption values [11]. This mixed-mode as well as actual cases of fragmentation and lamina bending modes are illustrated in Figure 2-6.

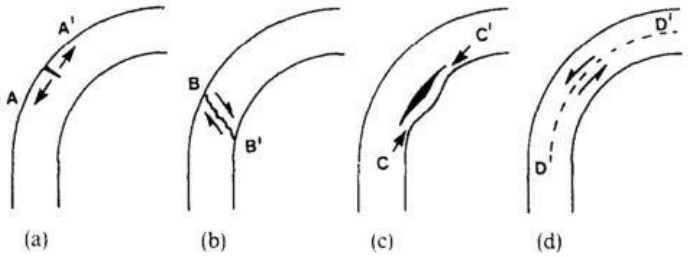

Figure 2-5. Failure modes producing fronds fracture. Tensile (a), compression/shear (b), buckling (c) and interlaminar shear (d). (Source: Hull [12]**).**

a) b) c)

Figure 2-6. Actual components failed by fragmentation (a) (Adapted from: Obradovic [26]**), lamina bending (b) (Source: Sun** [27]**) and brittle fracture (c) (Adapted from: Rabiee** [28]**).**

2.3 Parameters Affecting the Crashworthiness of Composite Tubes

As said before, several factors can affect the appearing of certain progressive failure mechanisms and therefore the crashworthiness response of the energy absorbers. Mamalis [4] identifies that materials, structural geometry and loading have an influence on the components' response. Apart from these, Rabiee [11] and Lau [16] also included, in their respective reviews, the trigger mechanisms as features affecting the components crashworthiness. Many authors report experimental and numerical work dealing with these topics. Details on these

effects are approached in the following sections with a special focus on trigger mechanisms.

2.3.1 Trigger Mechanisms

As introduced previously, trigger mechanisms are geometrical features added to the energy absorbers to act as stress concentrators. This initiates the component's progressive collapse thus preventing its global and catastrophic failure [11]. Several authors have worked on these elements dealing composite tubes [12,13,16,24,29–34] and their influence on the crashworthiness performance of the components is well-recognised. Investigated and most widely reported triggers are included in Figure 2-7. These are mainly: bevel/chamfer, steeple/double chamfer, plug, tulip, notch and ply drop off. More complex solutions can be found such us the SMA (Shape Memory Alloy).

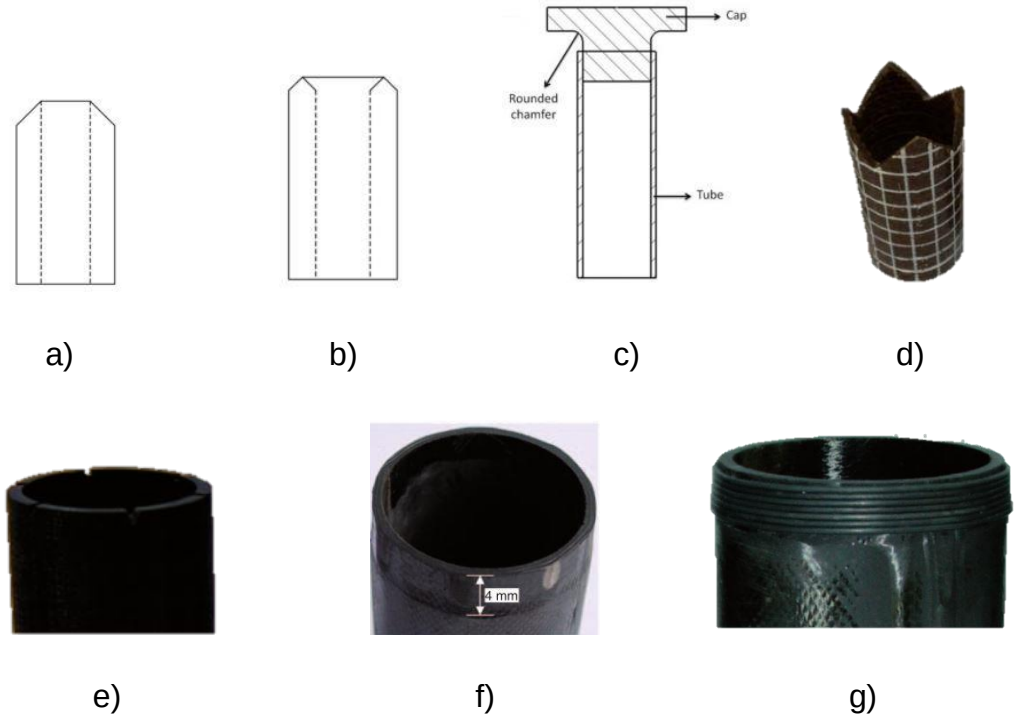

Figure 2-7. Trigger mechanisms on composite tubes investigated in the literature. Bevel/chamfer (a) (Adapted from: Rabiee [11]**), Steeple/Double chamfer (b) (Adapted from Rabiee** [11]**), Plug (Adapted from Tong** [34]**), Tulip (d) (Adapted from Sivagurunathan** [16]**), Notch (e) (Adapted from Tong** [34]**), Ply drop off (f) (Adapted from Huang** [32]**) and SMA (Adapted from Huang** [32]**).**

Czaplicki [29] and Jiménez [33] studied squared section tubes with chamfer and tulip triggers in E-glass composites. Czaplicki [29] reported that tulip triggered tubes showed higher values of energy absorption than the chamfered ones. Moreover, tulip triggered tubes showed a smooth force response without initial peak when compared to the bevel ones, as shown in Figure 2-8. These results are aligned with the ones from Jimenez [33] who also found smooth loading curves for tulip triggers but found less difference among the absorbed energy results compared to bevelled tubes. However, it was proved the strong effect of the chamfer angle on the crashworthiness response, reporting differences up to 25% with best EA results for 60º when compared with 30º and 45º. This angle dependence was less evident for the tulip triggered tubes.

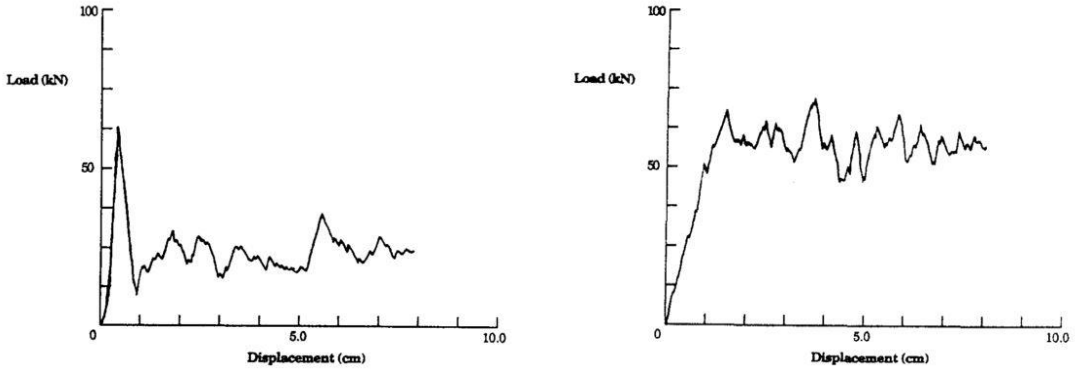

a) b)

Figure 2-8. Comparison of the crushing response of a bevel triggered (a) and a tulip triggered tube (b). (Source: Czaplicki [29]**).**

Palanivelu [30] compared 45º bevel and tulip triggers in circular and squared E-glass tubes. The triggers were found to behave differently in the two different cross-sections. For squared sections, the tulip was found to drive to higher energies than chamfer. Contrary, for circular sections, chamfered tubes showed a better performance. That is explained due to the circumferential large delamination exhibited on the circular tubes that was promoted by the chamfered trigger which is geometrically more homogeneous than the tulip one. However, tulip triggered appeared to be more suitable for the crushing response of box-

section tubes, what is aligned with the results mentioned previously of Czaplicki [29].

The rest of the investigated authors dealt with circular section tubes only, which have been proved to be more efficient than the square ones as described later on in section 2.3.2.1. Hull [12] reported the use of 45º chamfers and anticipated that different chamfer angles may produce changes in the tubes' initial crushing. This effect was justified by Farley [24] by means of a certain tube length influenced by the triggers during the initial stages of the crushing response until it is stabilised. Farley [24] also described the phenomena around 60º bevel triggers stating that normally these stress concentrators will produce local failure by means of small cracks which are affected by the wall thickness too. However, ductile composites will show plastic deformation around the triggers.

Sivagurunathan [16] explored the crushing behaviour of natural fibre tubes using four different initiators: no trigger, chamfer, double chamfer (steeple) and tulip. Tubes with no triggers failed catastrophically as expected and driving to very poor values of SAE. Triggered tubes showed a brittle fracture failure mode. Tulip triggered tubes performed the best under all the main crashworthiness variables. Small differences in peak loads were reported as well as very important differences in mean forces which produced this difference in the SAE. This difference in conclusions with Palanivelu [30] can be produced by the difference in the crushing modes promoted by the fibres used. As in the case of box tubes [29,33], tulip triggered tubes did not exhibit an initial peak in load, also they provided the best results in terms of SAE. Finally, among the single and double chamfered tubes, the second showed around 20% improved SAE with increased mean force and similar peak force.

Atthapreyangkul [13] reported the effect of different end conditions on plug triggered CFRP tubes as well as the influence of the plug radii. The critical radii producing a significant drop in performance if exceed was found at 2.7 mm. The effect of the plug radii was found to be less significant in thicker tubes (3 mm wall thickness) than in thinner tubes (2 mm wall thickness). This was justified by the reduction in the number of fronds formed which reduced the friction effects and

enhanced the fracture ones making the process less dependent on the plug type. Regarding the end configurations, best EA results were found for non-chamfered tubes, whereas the initial peak load was avoided by using inward folding.

Tong [34] tested a different plug type with a semi-circular shape (Figure 2-9). It showed a stable crushing behaviour and therefore was found to be eligible for crashworthy components. However, a two stages initial loading response was found. This effect was vanished by introducing also notch triggers in the tube end (Figure 2-10) which did not influence significantly the SAE results. The plug radii were changed in the range of 5-10 mm showing that smaller radii lead to better SAE and shift the crushing mechanism from splaying to fragmentation. These results on the radii effect are similar to the ones from Atthapreyangkul [13] but in a different radii range. Tubes made out of fabric materials were also tested achieving the SAE value of 101.7 kJ/kg.

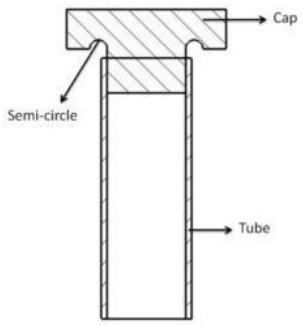

Figure 2-9. Description of the semi-circular plug type trigger tested by Tong [34]**. (Adapted from Tong** [34]**).**

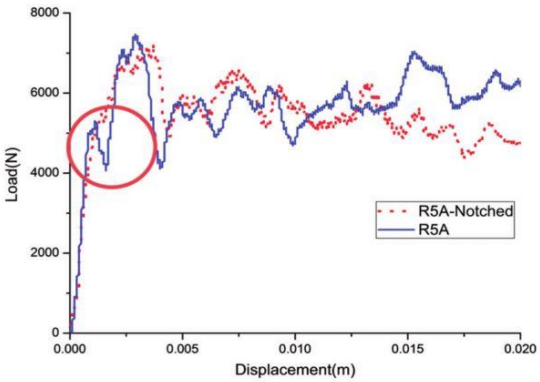

Figure 2-10. Effect of the addition of notch triggers to plug type crushed CFRP tubes. (Source: Tong [34]**).**

Finally, Huang [31,32] reported the use of two engineered triggers in CFRP components. First, bevel and crown (a combination of bevel and notch trigger as shown in Figure 2-11) were compared. Crown triggered specimens revealed a loading response with an initial drop followed by a further increase, as happened in the plug triggered tubes of Tong [34] before introducing the notches. This reveals that notches combined with plug triggers produce more stable results than when they are combined with bevel triggers. Also, similar mean forces and SAE were obtained for the crown and the simple chamfer triggers with a reduced peak force for the crown tubes.

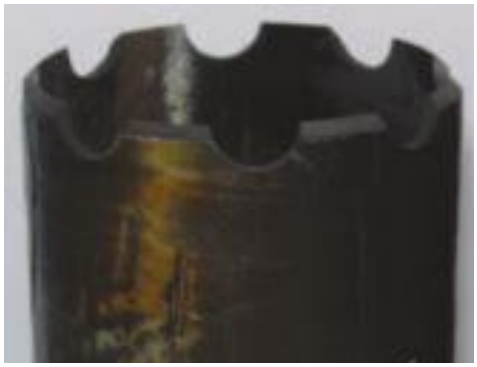

Figure 2-11. Detail of the crown trigger suggested by Huang [31]**. (Adapted from Huang** [31]**).**

Huang [32] also compared the ply drop off trigger with a radically different solution involving the use of a Shape Memory Alloy (SMA). This new solution exhibited very high SAE values around 100 kJ/kg compared to the around 80 kJ/kg of the ply drop off triggered tubes. This solution, however, involves the use of more materials and adds more complexity to a problem that is already complex by nature.

As the main conclusion, the use of triggers has been proved to be required to achieve progressive and stable mechanisms thus avoiding the catastrophic failure of the components. In fact, in the work of Hosseini [6], a great number of unstable results are obtained what could be due to the fact of not using triggers at the structures.

Summarising, the trigger mechanism effect has been proved to be a widely studied topic showing however still a lot of challenges in terms of characterisation. Also, it has been shown how the same triggers will lead to different results for different tubes' shapes, laminate materials, tubes' wall thickness and depending also on the particular crushing mechanism that takes place. Therefore, conclusions from these studies should be taken carefully and extrapolations should not be done. In order to predict the performance of a certain trigger, results from similar experiment conditions (in terms of these mentioned variables) should be taken into consideration. Nevertheless, this broad overview was required to fully understand this complex problem and analyse all the mentioned influences.

2.3.2 Other Parameters

Despite being trigger mechanisms the main object of this project, the influence of other parameters will be briefly described in the following sections to get a better understanding of the complex crushing mechanism of composite components.

2.3.2.1 Tube Geometry

Different geometries and sections are reported in the literature. These geometries are straight, pyramidal/conical section, stepped conical and corrugated. Different sections such as circular, square and H have been studied as well. Section properties such as thickness and t/D or D/t ratios (thickness to diameter or vice versa) have been studied as well.

Zhang [35] reported that conical tubes lead to lower EA capabilities than circular straight tubes. Also, it was noted that the bigger the cone angle is, the lower the resultant SAE will be. Palanivelu [36] tested circular tubes with conical (CC-X,Y), stepped conical (HG-A,B) and corrugated (HG-X,Y) tubes as shown in Figure 2-12. Results depicted that conical tubes behave better than stepped conical which, however, lead to better results than the corrugated ones.

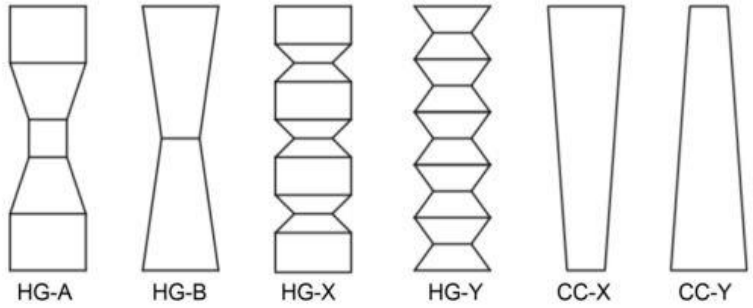

Figure 2-12. Description of the circular tubes tested by Palanivelu. (Source: Palanivelu [36]**).**

Concerning to sections, Jiménez [33] reported that regardless to the triggers induced, square sections behave slightly better than H sections in terms of SAE. Also, H section tubes produced a 15% drop in SAE, but a 60% in peak force. Palanivelu [36] and Zhang [35] concluded that circular tubes lead to higher SAE than square sections. Several authors reported the effect of section properties such as wall thickness and t/D ratio [4,13,25,35]. They all concluded that the bigger the t/D ratio is, the higher SAE is obtained. Within this increase in t/D, Farley [25] identified that a shift from splaying to fragmentation mode occurred, existing an upper limit for the t/D which produces a drop in SAE. Mamalis [4] found that this relation between t/D and SAE is not linear for CFRP composites and changes for different diameters. Atthapreyangkul [13] found that bigger thickness will reduce the influence of the trigger shape in plug-type triggered tubes. The t/D ratio to obtain stable results has been identified in the 0.015-0.25 range, being values lower than 0.015 resulting in global and sudden failure rather than progressive [11].

2.3.2.2 Fibre Properties

Most widely reported fibres are carbon [13,17,25,27,28,31,37,38], glass [25,30,33,35,36,39,40] and aramid [12,24,25,41]. Mamalis [4] stated that CFRP tubes exhibit higher values of SAE than aramid and glass tubes. Farley [24] studied the influence of the fibre properties on the crushing mechanisms, stating that the stiffer the hoop fibres are, the shorter will be the interlaminar cracks promoting the transverse shear failure mode to occur. Natural fibres such as jute

[16] and flax [8] have been tested proving their suitability for crashworthiness purposes but showing SAE values between 30 [16] and 41 [8] kJ/kg.

2.3.2.3 Matrix Properties

Most widely reported resins are epoxy [17,25,27,28,31,35–37,39], polyester [12,30,33,40] and, less extensively, vinylester [30,40]. Farley [24] described the likelihood of the mode I and mode II cracks to grow depends on the matrix toughness. Mamalis [4] described the large values of SAE (180 kJ/kg) that can be obtained using PEEK (thermoplastic) resins in quasi-static loadings, however in dynamic cases this performance drops significantly as showed by Lavoie [41].

2.3.2.4 Strain Rate

Farley [24] stated that the influence of this parameter depends on the failure mode taking place. Transverse shear is a mode driven mainly by the bundle fracture which depends on the fibres strength. Fibres are normally not sensitive to strain rates. Therefore, tubes failing under this mode will have low sensitivity to the strain rate. However, splaying mode is driven by the cracks opening, lamina bending and friction. In the cracks opening both fibres and resins interfere, so higher strain rate dependency should be found. Also, friction coefficients can vary between static and dynamic conditions [24].

2.3.2.5 Temperature

Similar results are found in terms of temperature effects as for strain rate. This variable affects mainly the resin properties. Mamalis [4] reported a strong influence in the crushing process when the temperature goes over 0ºC.

2.3.2.6 Fracture Toughness

Ghassemnejad [38] studied this effect in CFRP hybrid (combination of UD and fabric laminas) components. The relation among fracture toughness both in mode I and II (G_{IC} and G_{IIC}) was proved, showing that hybrid configurations with higher fracture toughness resulted to be better energy absorbers. This same idea was also described by the same author for UD laminated tubes [39]. To enhance this relation, Rabiee [28] proved with positive results the effect of stitching to increase the fracture toughness. Warrior [40] also recognises the influence of the fracture

toughness in the SAE, however states that a balance between interlaminar and in-plane properties is required. Z-pins insertion was tested revealing that the increase in fracture toughness produces a decrease in SAE due to the in-plane induced damage.

2.3.2.7 Laminate Design

Related to the previous section, Bin Mohamed [42] and Tao [43] studied the fibre angle relation with fracture toughness for CFRP laminates in mode I and mode II respectively. Both concluded that best results are obtained for 0º/0º interfaces. Moreover, Tao [43] proved that the bigger the angle θ in (0º/θ) interfaces is, the lower the mode II fracture toughness results. Regarding tubes' layup, Ghasemnejad [39] found similar SAE results for E-glass square tubes with (0º/θ) interfaces and significantly lower for (-60º/60º) interfaces. Farley [25] found different angle influence for [0/±θ] laminate tubes from different materials. Mamalis [4] reported better performance of $[45/45]_n$ than in $[0/90]_n$ tubes. In a dynamic test of $[0_2/\pm\theta]$ laminate tubes, it was found that the bigger θ, the bigger SAE. Mamalis also reports results from other authors driving to different conclusions than the ones from Farley [25].

Regarding the lamina's architecture, the use of both UD and 2D woven are found in the literature. Values found for tubes composed of CFRP UD laminas are 25 kJ/kg [34], 50 kJ/kg [17], 60 kJ/kg [31], 75 kJ/kg [13] and 60-100 kJ/kg [32]. On the other hand, tubes made out of CFRP woven fabrics are reported to exhibit SAE values of 55 kJ/kg [17], 60-100 kJ/kg [34] and 66 kJ/kg [26].

2.4 Numerical Modelling of Composite Crushing Tubes with LS-DYNA

The numerical analysis of the crushing behaviour of composite components has been carried out by several authors [7,17,26,37,38,44,45]. LS-DYNA is the most widely reported software used to analyse the crashworthiness response of composite components [17,26,35,38,44,45]. It is a commercial explicit solver conceived for non-linear dynamic and impact problems [17]. Also, other software

such as ABAQUS [7] and MSC Dytran [37] have been used to study this problem by other authors.

Among these, Zhang [35] and Ghasemnejad [38] studied quasi-static problems where it was required a mass scaling to reach the quasi-static conditions and increase the time-step size to reduce computational costs. Hussain [44], Bisagni [17], Obradovic [26], and Chatla [45] analysed problems driven by the initial impactor's mass and velocity i.e. impact cases. All these reported the use of quadrilateral shell elements to model the energy absorbers, being the Belytschko-Tsay [17,26,45] and the Belytschko-Lin-Tsay [38,44] the shell element types used. Zhang [35], Chatla [45] and Ghasemnejad [38] reported element sizes ranging from 2.5x2.5 mm to 3x3 mm. Regarding the simulation of the tube's laminate, some authors opted for single layer with given laminate properties [35,44], others for multi-layered single shells representing the laminate sequence [17,26] and some others for two shells models representing two half laminates bonded either with cohesive elements [45] or with an "*AUTOMATIC_SURFACE_TO_SURFACE_TIE_BREAK" contact definition [35,38]. This last option allows simulating the central crack in lamina splaying cases. Boundary conditions of the support end of the tubes have been found to be either fixed conditions [38,44,45] or constrained by a rigid plate acting as a static wall [17,26,35]. The impactor is commonly modelled either by a rigid body (2D [35,44] or 3D [38]) or by using the LS-DYNA rigid wall option (planar and moving) with allocated mass and initial velocity [17,26,45]. Different solutions are found to define the contact between the impactor and the specimen. Bisagni [17] and Obradovic [26] used the "*AUTOMATIC_SURFACE_TO_NODE" contact definition. Ghasemnejad [38] made use of the "*AUTOMATIC_NODES_TO_SURFACE" contact law and finally Zhang [35] used the "*AUTOMATIC_SURFACE_TO_SURFACE" one. Regarding the contact definition to prevent the self-penetrating of the tube with itself, all reported solutions made use of "*AUTOMATIC_SINGLE_SURFACE" contact. The LS-DYNA material card most widely reported is the 54 (*MAT_ENHANCED_COMPOSITE_DAMAGE) [35,38,45] which includes the Chang-Change failure criteria. The use of Material 55 [17] which is equal to

Material 54 but using the Tsai-Wu failure criteria and Material 58 [44] (*MAT_LAMINATED_COMPOSITE_FABRIC) has been reported too. In some of these works, comparisons between numerical and experimental results were performed, leading to errors of 15% [44], 20% [17] and 10% [38] for peak force, of 5%[44], 6.5% [17] and 10% [38] in mean force, of 2-9% [26] in crushing distance and 5% [35] in SAE.

3 PHASE 1 – MATERIALS AND MANUFACTURING

3.1 Specimens and Process Description

This section introduces the 3 specimens that were analysed in the first stage for the triggers characterisation and the FEA model validation. Also, it describes in detail the manufacturing process that was undertaken to produce the tubes and to introduce the triggers. Manufacturing was performed at the Enhanced Composites and Structures Centre, Cranfield University.

A single tube was manufactured by hand layup over a 500 mm long metallic mandrel. The mandrel was turned on a lathe up to getting a final OD of 65.2 mm. This process, apart from serving as a diameter correction, enhanced the surface finishing of the mandrel which resulted crucial to ease the tube's releasing from the mould after curing. Once the tube was laminated, cured and released, it was cut to provide the three tubular specimens of 150 mm each. After that, the triggers were machined on them.

3.1.1 Composite Material

The tubes were made from MTC510-UD300-T700 carbon/epoxy unidirectional prepreg laminas. The material mechanical properties are included in Table 3-1, and were provided by the material supplier, SHD Composites [46]. Lamina's nominal thickness after curing is 0.3mm with an areal density of 300 gsm.

Table 3-1. Mechanical properties of MTC510-UD300-T700 carbon/epoxy laminas.

MTC510-UD300-T700 Lamina Mechanical Properties [47]					
Elastic Properties		**Strength properties**			
E_1 (GPa) (+)	119.3	X_t (GPa)	2.282	e_{ft}*	0.019
E_2 (GPa) (+)	8.2	X_c (GPa)	1.067	e_{fc}*	0.009
E_1 (GPa) (-)	113.6	Y_t (MPa)	54.0	e_{mt}*	0.007
E_2 (GPa) (-)	9.3	Y_c (MPa)	200.0	e_{mc}*	0.022
G_{12} (GPa)	3.6	S_{12} (MPa)	99.0	e_{ss}*	0.028
v_{12}	0.34	ILS (MPa)	84.8		
v_{21}	0.01				

*Strains at failure were calculated from the failure stresses and elastic modulus at the corresponding directions.

3.1.2 Specimens Parameters

For the experimental phase, 3 tubes were manufactured for the triggers characterisation and FEA model validation. The tubes were manufactured with a [45/-45/0/90]s stacking sequence of UD carbon/epoxy laminas. The 0 degrees plies were oriented parallel to the tube longitudinal axis.

The outer diameter of the tubes was 70 mm with a wall thickness of 2.4 mm, providing a t/D ratio of 0.034 which according to Rabiee [11] fits within the range of ratios providing stable axial crushing.

Two different triggers and two different trigger configurations were analysed by means of that specimens. The triggers were 30º and 60º bevel and 60º tulip. This provided valuable results for both an experimental comparison and to test the reliability of the FEA model in a wide range of conditions.

3.2 MANUFACTURING PROCESS

3.2.1 Composite Manufacturing

As introduced before, the process consisted of a hand layup of the several composite laminas over a metallic mandrel of 65.2 mm outer diameter and 500 mm long. This mandrel was turned on a lathe to adjust its size and improve surface finishing.

3.2.1.1 Mould Preparation

The first stage of the process was to apply 4 layers of release agent over the mould to ease the tube removing once cured. The product used was Chem-Trend Chemlease® PMR 90 EZ. Figure 3-1 shows the mandrel once the releasing solution was applied.

Figure 3-1. Metallic mandrel used as a mould for the tube's manufacturing.

3.2.1.2 Layup Process

The composite material was provided in a 300 mm width roll where the 8 laminas required for the layup were extracted from. Each lamina was trimmed with different width according to the tube's OD at each stage of the laminating process. The laminas' length was 480 mm to leave some gap with the mandrel edges in order no ease the tube releasing. Layup and laminas details are included in Table 3-2.

Table 3-2. Laminas dimensions.

Layer	Ply orientation	Starting OD (mm)	Ply thickness (mm)	Laminated OD (mm)	Lamina length (mm)	Lamina width (mm)
1	45	65.2	0.3	65.8	480	204.8
2	-45	65.8	0.3	66.4	480	206.7
3	0	66.4	0.3	67.0	480	208.6
4	90	67.0	0.3	67.6	480	210.5
5	90	67.6	0.3	68.2	480	212.4
6	0	68.2	0.3	68.8	480	214.3
7	-45	68.8	0.3	69.4	480	216.1
8	45	69.4	0.3	70.0	480	218.0

Once all laminas were tailored, they were rolled over the mandrel. First layering process is shown in Figure 3-2. A debulking process was performed after each lamina was laid up. To do that, the mould was covered by a release film and bagged into a sealed bag connected to a vacuum pump. This process, Figure

3-3, was carried out for 15 minutes for every layer but for the last one which was left over two hours. This debulking process enhanced the consolidation among the layers and removed any gap or wrinkle among them. After that, the next layer was added and this process was repeated until the full lay-up was laminated. The tube after the full lamination is shown in Figure 3-4.

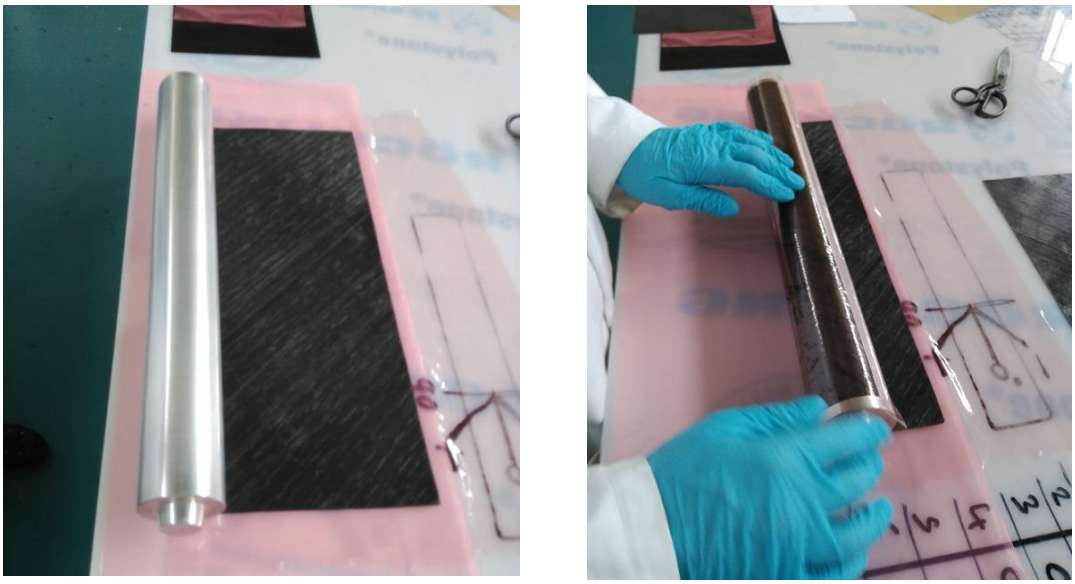

a) b)

Figure 3-2. Laminate process layout, (a) and laminating procedure (b).

Figure 3-3. Debulking process set up.

Figure 3-4. Tube after the laminating process.

3.2.1.3 Curing

Once the tube was layered up and after the last debulking process, the tube was un-bagged to set it up for the curing. The curing process was carried out in an oven applying vacuum to the bagged tube which was kept vertically by means of a stand. To set it up, the release film was kept around the specimen. Over this one, a peel ply was used to allow the breathing during the curing (Figure 3-5). Top end was covered with this material too (Figure 3-6 (a)), creating a hat to prevent resin to come out which would difficult tube's releasing. Some insulating material was used to create a stable mat in the bottom end (Figure 3-6 (b)). Then, all this was bagged and a vacuum valve was inserted near the top end. Full set up before moving the tube into the oven is shown in Figure 3-7. As said before and shown in Figure 3-8, the tube was kept vertically during the curing. This position will ensure a good radial homogeneity of the tube.

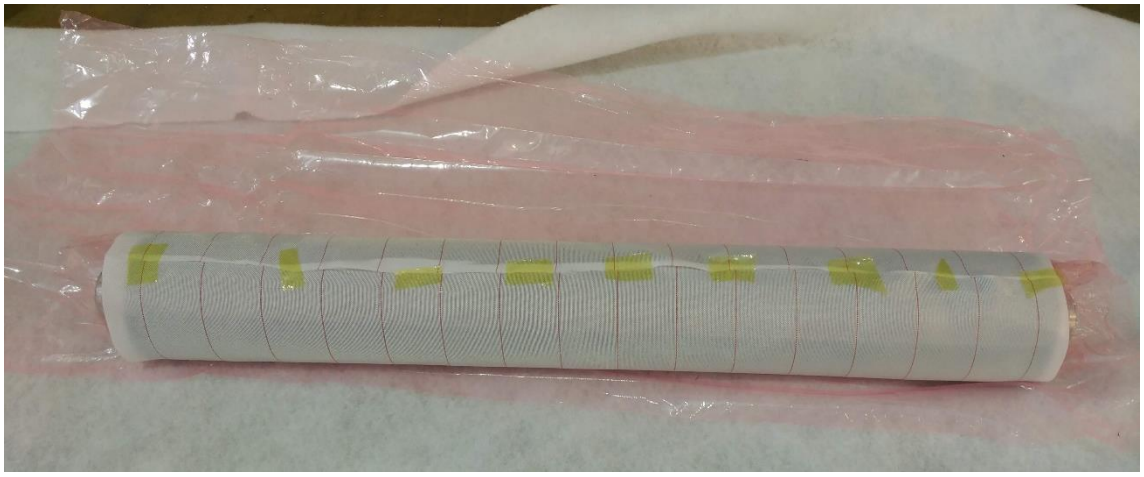

Figure 3-5. Tube covered with the peel ply material.

a) b)

Figure 3-6. Detail of the Bottom (a) and Top (b) ends of the tube during the curing setup process.

Figure 3-7. Tube setup for the curing process.

Figure 3-8. View of the oven's interior with the tube set up for curing.

The tube was cured under the following cycle: 1-2 ºC/min until 120 ºC + 1 hour @ 120ºC + 1.5 hour cooling. This cycle was selected as a trade-off between the MTC510 resin system rheological properties and the issue of the huge thermal mass represented by the metallic mould.

Once the tube was cured, and after refrigerating it for several hours to ease the releasing, it was taken out from the mould. The final outcome of the process is shown in Figure 3-9. As expected, the tube resulted with an OD of 70.0 mm, an ID of the mould of 65.2 mm and a rough length of 480 mm.

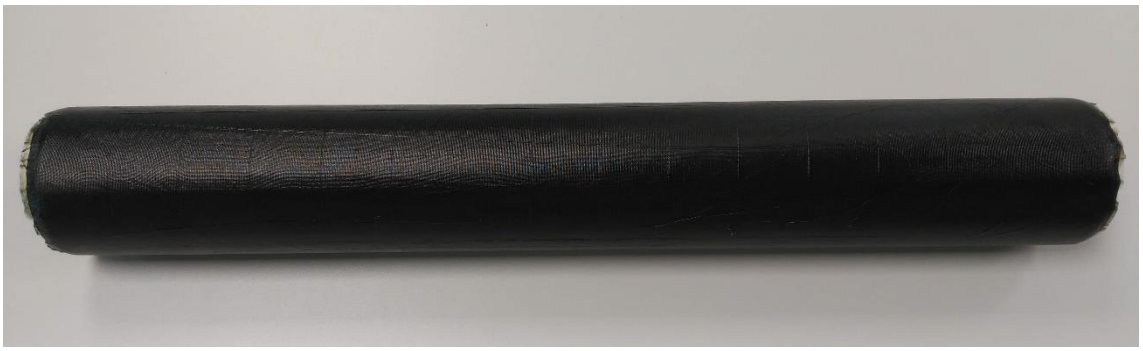

Figure 3-9. Cured tube released from the mould

3.2.2 Specimen's Cutting and Triggers Machining

As introduced previously in section 3.1, three tubes were extracted from the laminated. The baseline tube had a final length of 480 mm that was reduced up to 450 mm after cropping the edges to ensure good finishing and end's homogeneity. This tube was finally cut into three different parts of 150 mm each.

Three different triggers were machined in the three different specimens. Two tubes were chamfered at one end with 30º and 60º respectively as shown in Figure 3-10 (a) and Figure 3-10 (b) respectively. These angles were used to perform a comparison around the widely reported chamfer angle of 45º. The remaining tube was tulip end triggered with 4 tips at an angle of 60º as shown in Figure 3-10 (c). Tulip trigger was selected since as presented in the work from Sivagurunathan [16], Jiménez [33] and Palanivelu [30] (introduced in section 2.3.1) they are able to avoid the initial peak in load. This, as described in section 1.2, is critical for crashworthiness applications. Four tips were machined on the tube in the same fashion as these authors did. The 60º angle was selected in order to be the same as one of the chamfered tubes but not too small in order not to consume too much length of the tube. Furthermore, the angle of 60º in tulip triggers has been reported also by Jiménez [33] and Palanivelu [30].

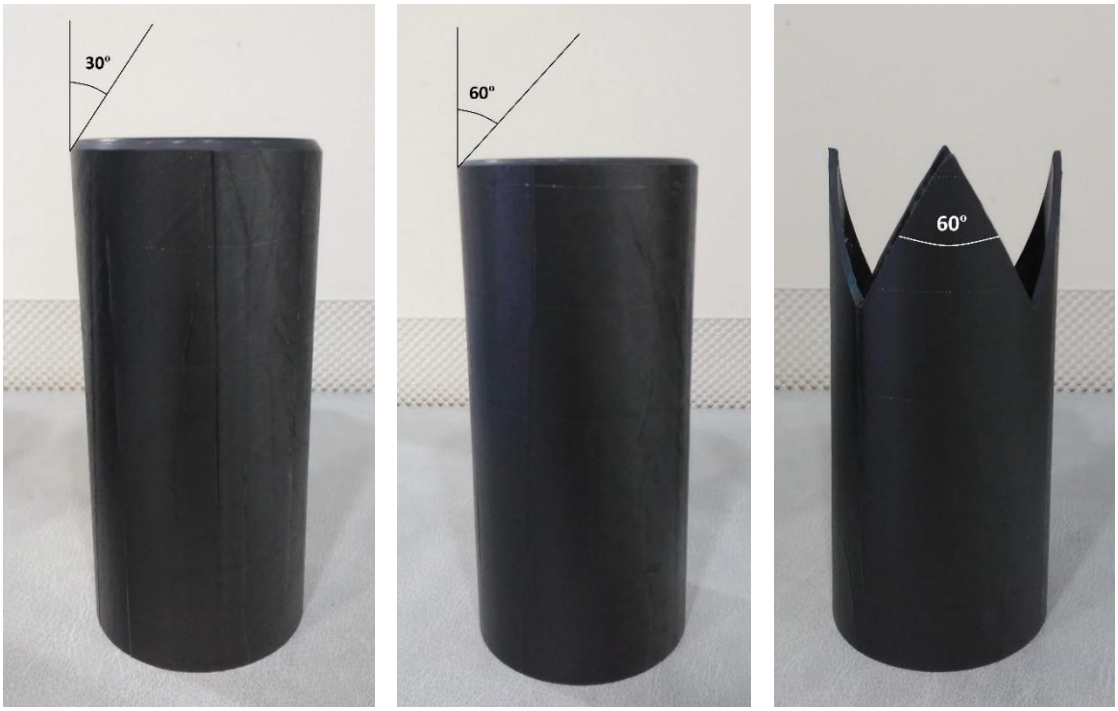

a) b) c)

Figure 3-10. Triggered specimens. Bevel at 30º (a), Bevel at 60º (b) and Tulip at 60º (c).

The selection of these triggers was a trade-off between simplicity and performance. Bevel triggers are simple to characterise, easy to manufacture and widely used. On the other hand, tulip triggers, despite being more challenging to manufacture, have been shown to reduce in some cases the initial peak in the force-displacement response. Justification and a better understanding of these two triggers can be found in section 2.3.1. A summary of the manufacturing results and final specimens' characteristics is included in Table 3-3.

Table 3-3. Summary of specimens' physical parameters.

	Specimen 1 – Bevel @ 60º	Specimen 2 – Bevel @ 30º	Specimen 3 – Tulip @ 60º
Specimen code	B60	B30	4T60
Stacking sequence	[45/-45/0/90]s	[45/-45/0/90]s	[45/-45/0/90]s
OD (mm)	70	70	70
ID (mm)	65.2	65.2	65.2
Wall thickness (mm)	2.4	2.4	2.4
t/d ratio	0.034	0.034	0.034
Length (mm)	151	150	148
Mass (g)	0.115	0.115	0.095
Density (kg/m3)	1494.2	1504.2	1259.4*

*Equivalent density assuming a cylindrical shape to simplify the SAE calculation.

4 PHASE 2 – SPECIMENS TESTING

The specimens were tested at the Cranfield Impact Centre (CIC) in a drop tower test rig. The CIC is an FIA certified laboratory specialised on impact testing and centre of inertia measurement.

4.1 Rig Description and Test Conditions

As mentioned, the specimens were dynamically tested in a drop tower rig, shown in Figure 4-1. This rig was chosen instead of the laboratory's sled to deal with smaller scale amounts of energy as at this stage, as the test results aimed mainly the validation of the FEA model and the triggers' characterisation.

Figure 4-1. CIC's drop tower rig used for the physical testing of the specimens

Tubes were vertically loaded by means of a flat impactor of 80 kg at 5 m/s thus producing an impact's kinetic energy of 1 kJ. Specimens' bottom end boundary conditions were simply supported. To protect the rig from a possible direct impact between impactor and rig's stand produced by a sudden failure of the specimens, those were surrounded by a piece of foam that would prevent this secondary impact, as shown in Figure 4-2 (a). Figure 4-2 (b) is included for visual purposes to clarify how the tubes went all the way through the foam and to show the support conditions. A 400kN load cell and an accelerometer were used to obtain the force-displacement response of the tubes from the test. The signal of the accelerometer was converted to obtain the impactor's displacement.

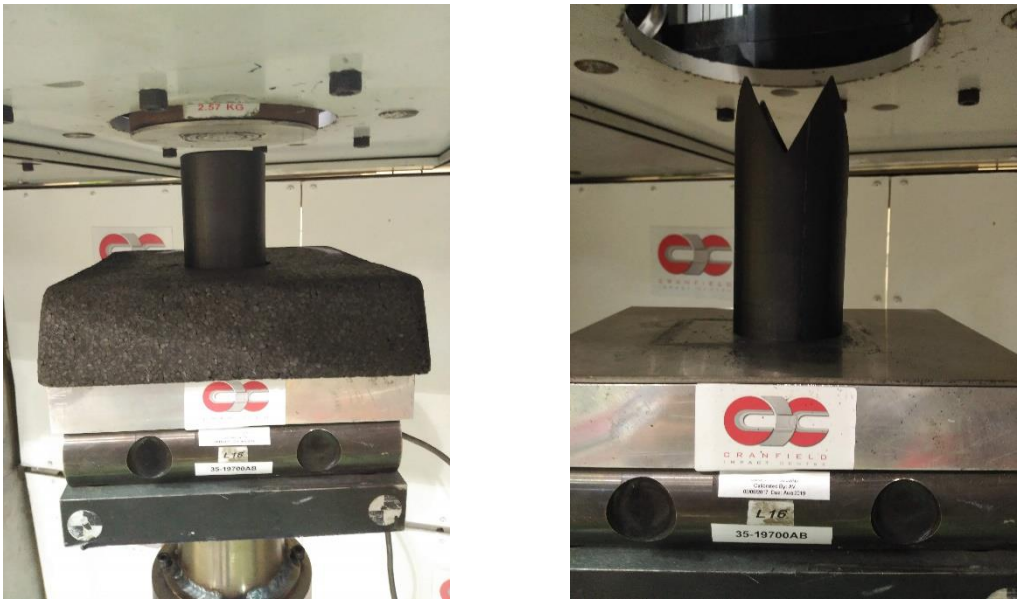

a) b)

Figure 4-2. B60 specimen and safety foam (a) and 4T60 specimen (b).

5 PHASE 3 – EXPERIMENTAL RESULTS ANALYSIS

Once the test rig and conditions have been described in section 4.1, this section presents and discusses the experimental results of the specimens testing. For the physical characteristics of this tube, Table 3-3 and Figure 3-10 are referred. It is important to remind here the stacking sequence of the tubes which was [45/-45/0/90]s since it will be referred throughout the results analysis.

5.1 Specimen 1 – Bevel at 60º (B60)

Figure 5-1 and Figure 5-2 show the tube after the impact test. Both figures depict that the tube failed progressively from the top (triggered) end throughout a brittle fracture mode but with a predominant lamina bending or splaying mode rather than a fragmentation one. Mode I circumferential main crack appeared in the outer 0º//90º interface producing therefore an inner bundle which is coarser than the outer. This failure might be motivated due to the fact that the UD 90º//90º laminate's middle interface is stronger in terms of fracture toughness (as reported by Bin Mohamed [42]) than the 0º//90º which actually triggered the cracking. Crumpled 90º fibres produce a debris wedge along the interface of this circumferential crack. While the outer bundle shows a clear bending and petal formation within the 0º fibres, the inner one depicts a larger amount of fibre fraction mode. Therefore, since the failure mode was not a pure lamina bending, certain failure modes appeared within the bundles too. On one hand, the outer bundle shows a mode II delamination at the -45º//0º interface, longitudinal intralaminar mode III cracks promoting the petals formation and some fibre fraction at the 0º lamina produced by bending. The strong bending interaction between the outer 0º lamina and the impactor can be observed at Figure 5-3 which depicts how these fibres tended to support the impactor whereas the ±45º fibres tended to roll down the tube. This fact can also be explained with the difference of bending angle of these laminas seen in Figure 5-1. On the other hand, the inner bundle presented mainly a brittle fracture mode probably produced by the accumulation of material in the inner section of the tube as well as the friction against the impactor.

Figure 5-1. B60 specimen after impact testing. Overview.

Figure 5-2. B60 specimen after impact testing. Top view.

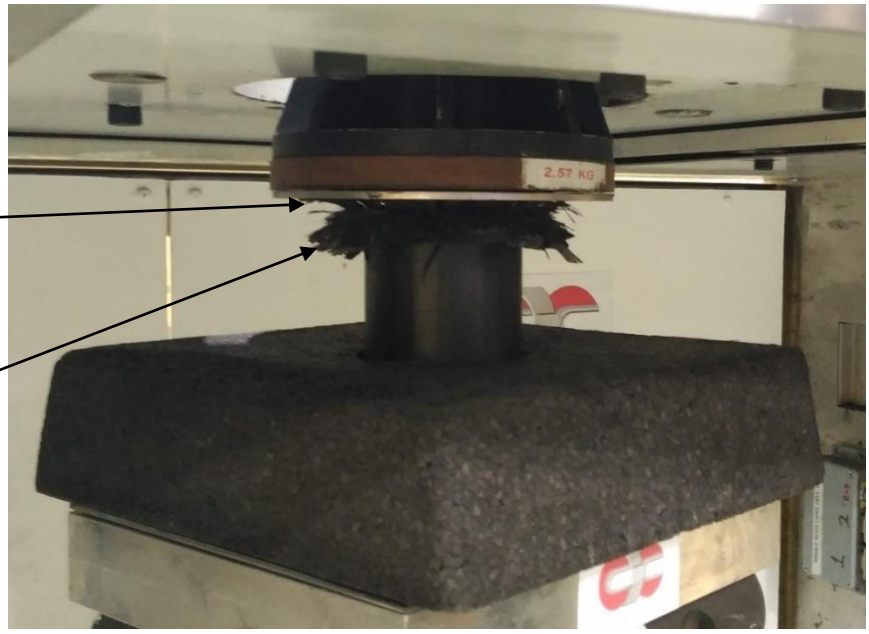

Figure 5-3. Detail of the B60 specimen just after the impact.

The force-displacement response of the specimen is included in Figure 5-9, whereas the main crashworthiness parameters collected in Table 5-1. The force pulse depicts an initial peak triggered at 89.9 kN followed by a drop in load and a sustained crushing force of around 30 kN. All the energy was absorbed within 34.6 mm, driving to a mean force of 28.9 kN and a SAE of 38.0 kJ/kg.

5.2 Specimen 2 – Bevel at 30º (B30)

Figure 5-4 and Figure 5-5 show the tube after the impact. Results are similar to the previous chamfered tube. The tube failed progressively from the top (triggered) end in a brittle fracture failure mode with predominant lamina bending. The main mode I crack is produced again at the outer 0º//90º interface. Again, crumpled 90º fibres produced a debris wedge along the interface of this circumferential crack. Similarly as the B60 specimen, the outer bundle exhibits a lamina bending failure mode, whereas the inner one presents a bent shape with fibre fraction. Furthermore, the outer bundle presents mode II interlaminar cracking at the -45º//0º interface, fibre fraction and petal formation at the 0º lamina due to longitudinal intralaminar cracks in mode III. On the other hand, as mentioned before, the inner bundle presents fibre fraction motivated by the

accumulation of material in the inner space of the tube and the high friction against the impactor.

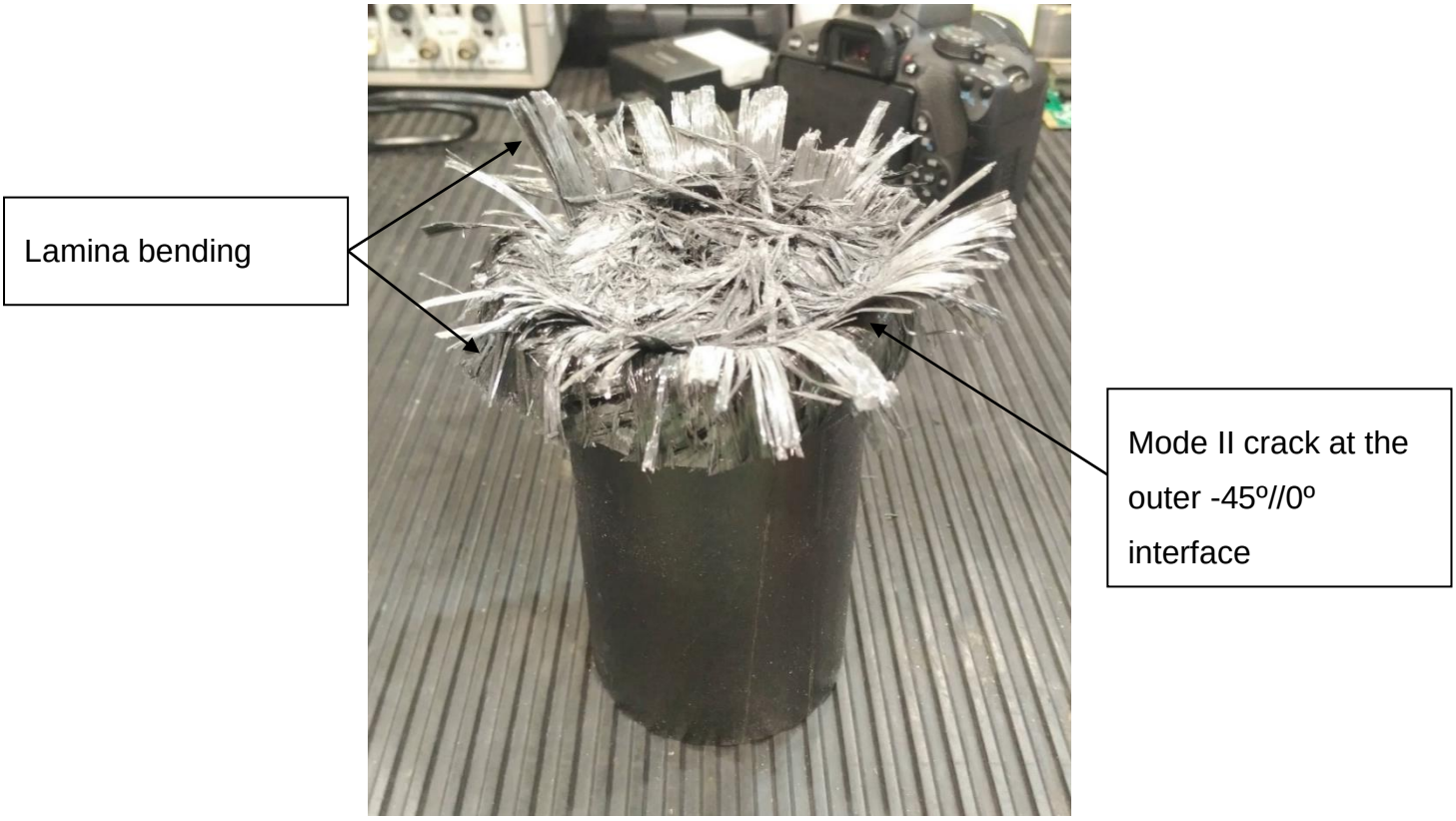

Figure 5-4. B30 specimen after impact testing. Overview.

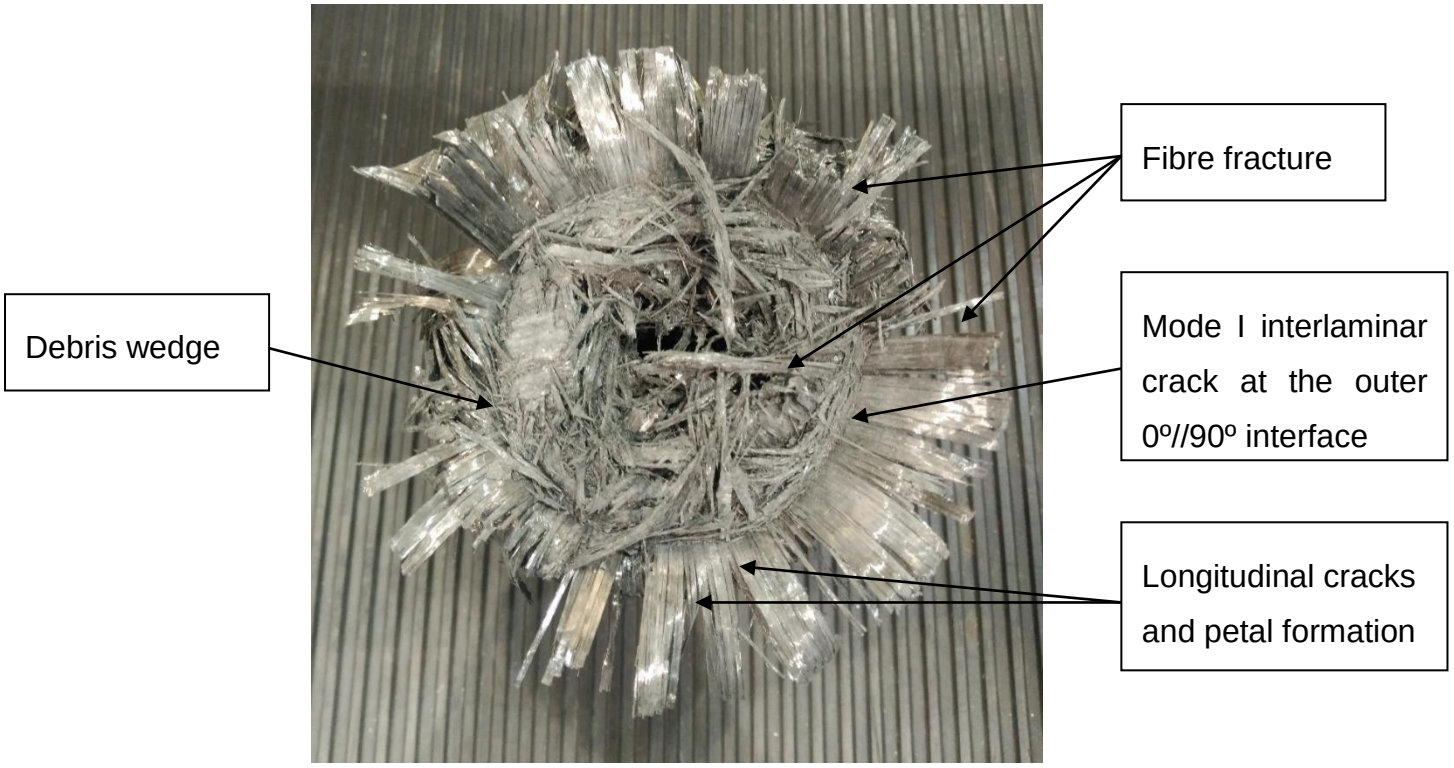

Figure 5-5. B30 specimen after impact testing. Top view.

The force-displacement response of the specimen is included in Figure 5-9, whereas the main crashworthiness parameters of it are collected at Table 5-1. The force pulse depicts a clear initial peak triggered at 71.8 kN followed by a drop in load and a sustained crushing force of around 30 kN. All the energy was absorbed within 32.5 mm, driving to a mean force of 30.8 kN and a SAE of 40.1 kJ/kg.

5.3 Specimen 3 – Tulip at 60º (4T60)

Figure 5-6 and Figure 5-7 show the tube after the impact test. Both pictures show that this tube failed by a brittle fracture mode, as the chamfered ones, but with a greater amount of fragmentation than those. The main central crack appears in mode I at the 0º//90º interface. Again, crumpled 90º fibres produce a debris wedge along the interface of this mode I crack. Regarding the bundles, the outer one shows fibre fracture at the 0º lamina and the mode II delamination at the -45º//0º interface exhibited by the chamfered tubes, is less evident here. Since this mode II delamination between the 0º and -45º laminas takes place in less amount, the longitudinal intralaminar cracks and petal formation at the 0º fibres

is also less evident. The inner bundle shows short fibre fracture due to the material accumulation in this area of the tube and the friction against the impactor.

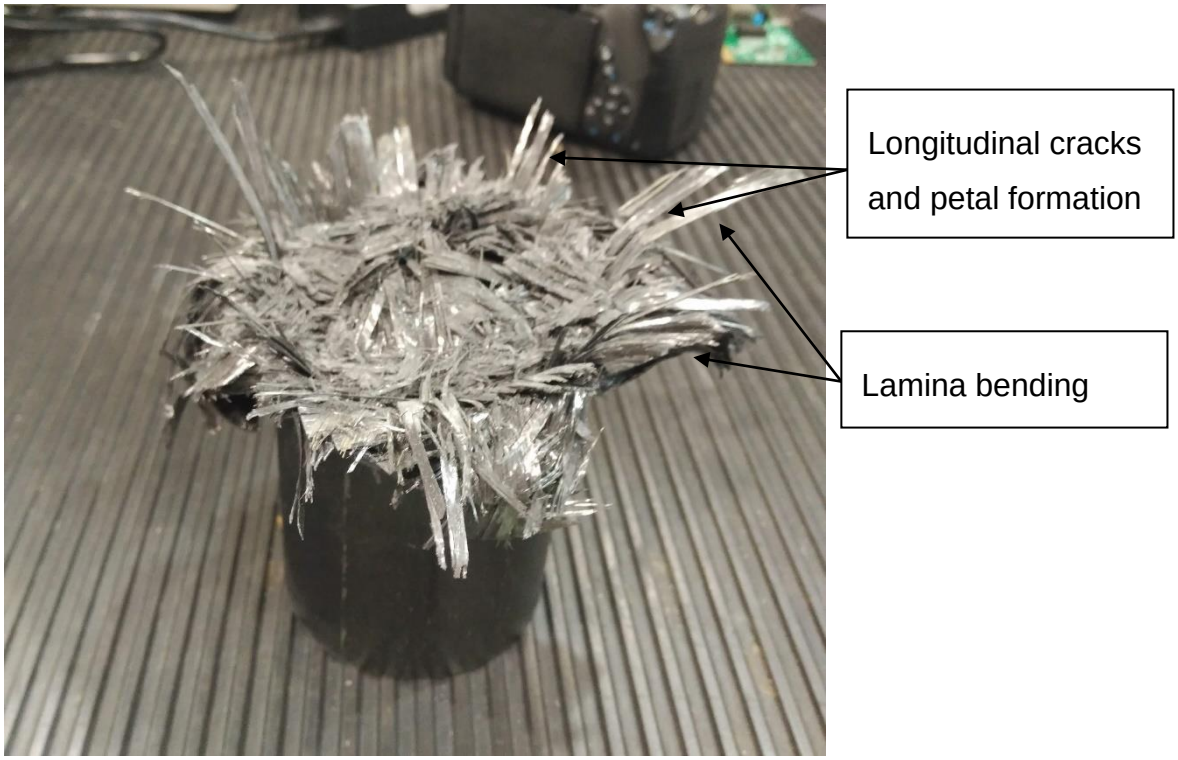

Figure 5-6. 4T60 specimen after impact testing. Overview.

Figure 5-7. 4T60 specimen after impact testing. Top view.

The force-displacement response of the specimen is included in Figure 5-9, whereas the main crashworthiness parameters of it are collected at Table 5-1. For this tube, load's rising is almost constant during the whole crushing scenario and seems to get stabilised once the full trigger (tube's tips) is crushed. This fact is motivated by the increasing tube's cross-section as the crushing progresses through the trigger. Therefore, the peak load is reached at the end of the load response at a value of 33.1 kN. All the energy was absorbed within 57.8 mm, driving to a mean force of 17.3 kN and a SAE of 37.1 kJ/kg.

Since the length of the trigger tips was around 47.6 mm, it can be said that the crushing was initiated along this length and then sustained progressively during the remaining 10.2 mm until getting to the final crushing of 57.8 mm. This short tube's progressive failure (just around 10 mm) is not enough to get a good understanding of how the failure is transmitted to the tube from the trigger once this one has completely failed. Also, it produced that approximately a 68% of the energy was entirely absorbed by the trigger which typically should act as failure initiator and not as energy absorption material, leaving only a 32% of energy to be absorbed by the tube itself. Nevertheless, if smooth force responses and

controlled loads are aimed, this trigger type can represent a good solution. Thus, this behaviour depicts that this trigger effectively gets rid of the initial peak load and can produce a smooth force response. This results together with the ones from other authors ([16,30,33]) prove this idea that was already anticipated before the testing and justified the use of this trigger.

5.4 Experimental Comparison

In general, the results showed a brittle fracture failure mode, similar to other authors' results who worked with similar materials, triggers, geometries and laminate designs [31,32]. This collapsing mode produced the failure mechanisms and features described by Hull [12] and Farley [24] which were introduced previously in section 2.2. Among these, the main mode I central interlaminar crack driving to the lamina bending, the debris wedge, as well as in-bundle failures such as mode II interlaminar cracks, fibre fraction and longitudinal intralaminar cracks are highlighted. Regarding tubes' geometry, the t/D ratio of 0.034 was proved to produce a progressive and stable crushing, as it could be anticipated from the 0.015-0.25 range to avoid catastrophic failure reported by Rabiee [11]. Regarding the SAE results (presented in Table 5-1), these are in the 27-40 kJ/kg range, which matches within the 25-100 range presented in 2.3.2.7 for CFRP UD laminated tubes. The reason why current results are not close to the top values of the 25-75 kJ/kg range could be because the main failure mechanism (mode I circumferential crack) took place in a weak interface such as the 0º//90º.

To ease the comparison, the crushed cross-section of the three tubes has been collected again at Figure 5-8. Regarding de chamfered tubes (B60-B30 specimens) a very similar brittle fracture failure mechanism was observed, as reported in sections 5.1 and 5.2. This one combined lamina bending and petals formation with several in-bundle failure mechanisms. However, looking at the tulip ended tube (4T60) less amount of petal formation is observed. In the bevel tubes, this phenomenon took place within the 0º lamina, which also delaminated from the -45º one. This in-bundle delamination did not happen in the same

amount in the tulip specimen, therefore making the longitudinal cracks that lead to the petal formation less likely to occur.

a) b) c)

Figure 5-8. Top view of the crushed specimens. B60 (a), B30 (a) and 4T60 (c).

Figure 5-9 shows the force-displacement response of the three tubes. As described before, bevel tubes presented the typical sharped load rising with a triggered peak load and following drop and load stabilisation. However, the tulip type tube presented a soft load rising within the trigger (tips) length followed by a constant load. Comparing the three tubes, it can be observed that the sustained crushing force of the three of them is very similar and around 30 kN. This gives consistency to the results and validates the manufacturing process. Comparing the bevelled tubes, it is clear that as the chamfer angle increases, the peak load becomes higher. This is produced since the bigger the angle, the flatter the top end, thus making more cross-section of the tube to face the impactor's surface offering more load-carrying surface. Regarding this angles comparison, results are opposite in trend as the ones presented by Jiménez [33] for square section tubes which could be due to the corners effect introduced by this kind of sections. However, current results seem to make sense if the approach of the trigger's cross-section facing the impactor and sustaining the load is applied. Furthermore, the B30 sample presented not only the benefit of producing a lower peak load, but also a higher mean force which produced a shorter displacement. Also, between these two tubes, a difference in the loading slope can be observed. The B30 specimen presents a slightly softer slope compared to the B60's one. This

makes the peak load duration to be longer. This fact should be assessed in combination with the load (and acceleration) levels, since (as explained in section 1.2) smaller peaks but sustained during a longer time could be as dangerous as higher peaks in shorter time periods.

Regarding the tulip ended tube (4T60), its initial force response depicts a completely different behaviour compared to the chamfered specimens as it did not present a rapid load rising followed by a peak and drop. Loading rising is almost constant during the whole crushing scenario and seems to get stabilised once the full trigger (tube's tips) is crushed. In fact, the load trends to the same value as the stable crushing force of the bevel tubes once the displacement passes the tips' length. As mentioned in section 5.3, this kind of response vanishes the initial and dangerous high peak force. This conclusion matches with the results presented by other authors that dealt with this kind of triggers [16,30,33] even taking into account the difference in materials, geometries and loadings.

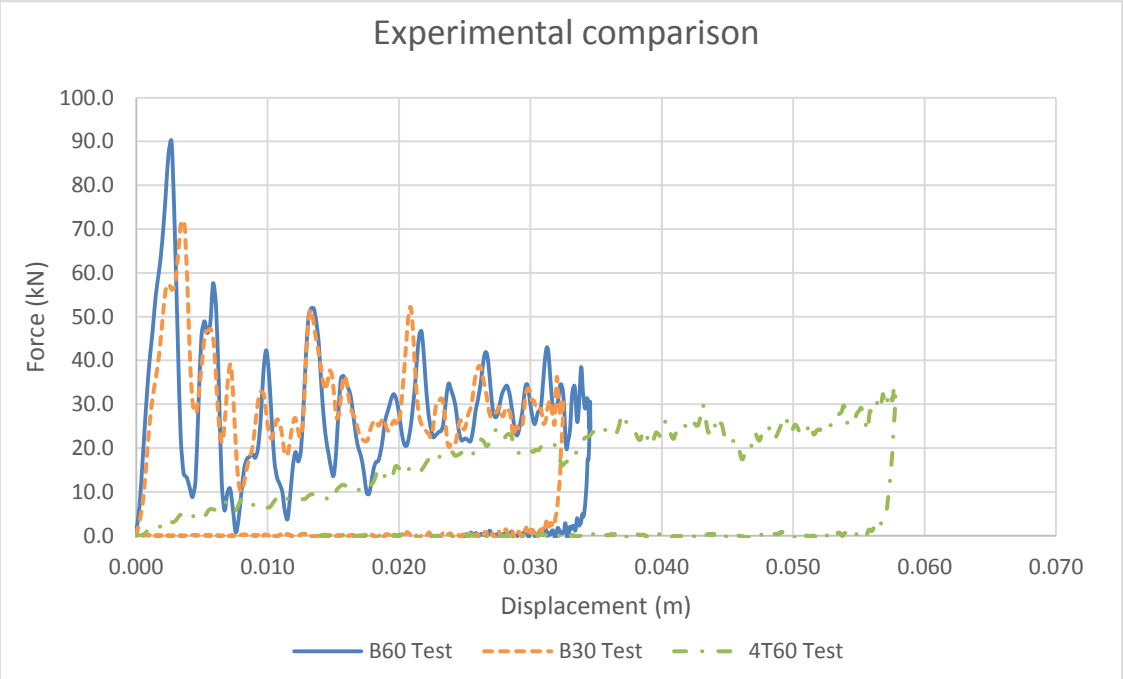

Figure 5-9. Specimens' experimental force-displacement responses.

The crashworthiness performance parameters of the specimens are collected in Table 5-1 and plotted and compared in Figure 5-10 and Figure 5-11. Regarding

the chamfered tubes and taking the B30 as a baseline, the B60 produced a peak load 25.2% higher than the B30 specimen. The 6% difference in mean force is translated in a 5.5% increase in SAE and 33.2% in CFE, showing that the tube with the 30º chamfer behaved better than the one with the chamfer at 60º. The increase in mean force is also represented in the increase in CFE from the B60 specimen to the B30. Therefore, due to the initial peak load reduction and for presenting higher values of SAE and CFE, the B30 specimen was concluded to perform better than the B60. Comparing these tubes with the tulip triggered one, it is clear looking at the figures that bevelled tubes produced higher forces than the tulip one. On one hand, the maximum force of 4T60 presented a 53.9% reduction compared to B30's. On the other hand, the mean force of 4T60 presented a 43.8% reduction when compared to B30's mean force. Also, the tulip specimen represented a slightly reduced (7.5%) SAE compared with the B30 specimen which obtained the highest value of SAE in the experiments. However, the fact of having lower load levels, produces an increase of 21.9% in CFE from the B30 specimen to the 4T60. Also, the larger value of displacement obtained for the tulip specimens, produces an increase of 77.4% in the SE parameter. Therefore, the tulip type trigger appears to perform worse in terms of mean force and SAE. Nevertheless, the reduction in peak force, the increase in CFE and SE, as well as the fact of avoiding the initial high peak load open the chance to, if the mean force can be improved throughout a trigger's tailored design which can accelerate the tube's loading, exploit the benefits that it brings.

Table 5-1. Specimens' experimental crashworthiness performance parameters.

	F_{max} (kN)	F_m (kN)	d (mm)	SAE (kJ/kg)	CFE (%)	SE (%)
B60	89.9	28.9	34.6	38.0	32.2	22.9
B30	71.8	30.8	32.5	40.1	42.9	21.7
4T60	33.1	17.3	57.8	37.1	52.3	38.5

The difference in SAE between the chamfered and tulip tubes could be explained by means of the macroscopic behaviour of the samples. Tulip tubes were reported (section 5.3) to produce a higher amount of fibre fracture and less amount of mode II delamination and longitudinal cracks at the outer bundle. This

reduces the energy absorption mechanisms to just the mode I central crack, the fibre fracture and the friction against the impactor. Therefore, per unit length, less energy absorption (failure) events took place in the 4T60 specimen producing lower load levels and making the tube to be less efficient.

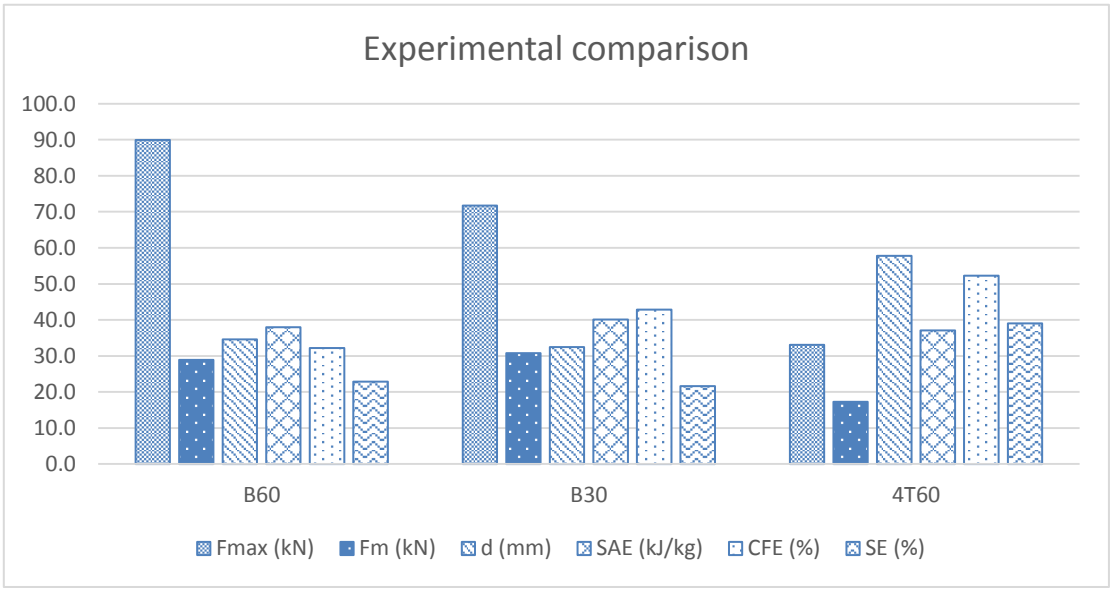

Figure 5-10. Specimens' experimental crashworthiness comparison. Grouped by trigger type.

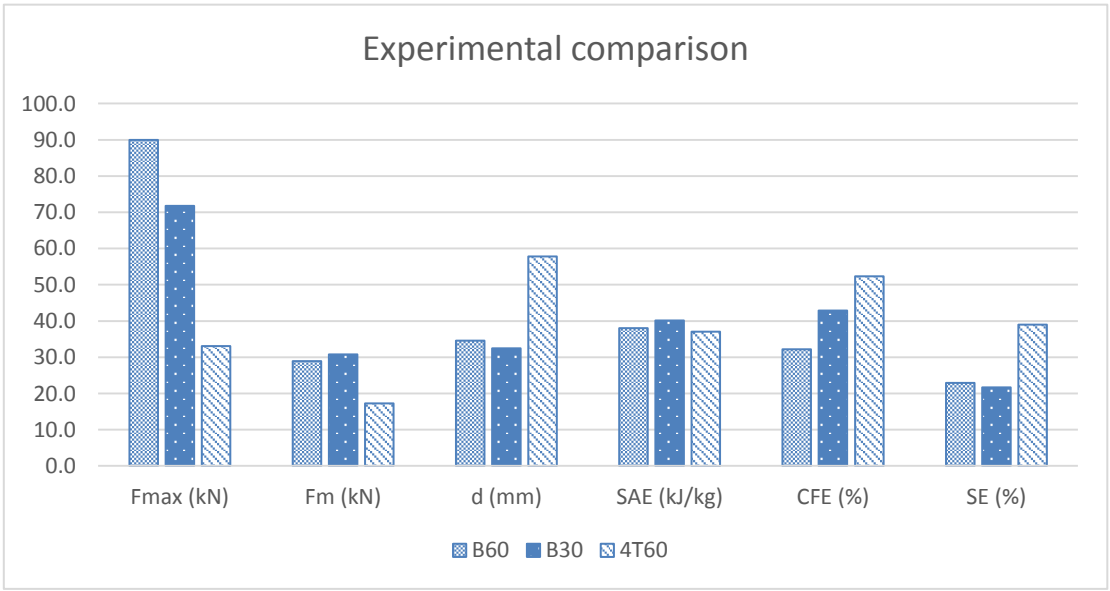

Figure 5-11. Specimens' experimental crashworthiness comparison. Grouped by performance parameter.

If weight reduction purposes are considered, the most important parameter would be the SAE. Figure 5-11 effectively depicts that B30 achieved the maximum value, followed by the B60 and the 4T60 specimens. Regarding the bevelled tubes comparison, this conclusion is aligned with the results from Jiménez [33] for square section glass tubes-polyester tubes. However, the maximum load trend with the chamfer angle differs with the one from this author. Also, regarding the comparison between the bevel and tulip triggers, current SAE results are aligned with the conclusions from Palanivelu [30], who tested glass tubes and found that for circular sections, 45º chamfer performed better than 60º tulip. However, Sivagurunathan [16] found for natural fibre circular tubes that 90º tulip triggered structures performed better than 45º chamfered ones. Therefore, conclusions are not straightforward and materials, geometries and triggers should be taken into consideration carefully.

6 PHASE 4 – NUMERICAL MODELLING WITH LS-DYNA

An FEM model was produced to enable a triggers redesign for the tube's optimisation without the need of undertaking several manufacturing and testing stages. The model was implemented in LS-PrePost 4.5 [48] and solved through LS-DYNA version R9.0 [49–51] which as previously mentioned, is a commercial code for solving non-linear dynamic and impact cases.

This model was developed to provide a tool to enable the numerical optimisation of the triggers. Therefore, the first stage of this numerical analysis once having the test results, was to create and validate the model to ensure a certain reliability for the upcoming component's redesign.

6.1 Model description

This section describes the final model set up that was proved to reproduce the actual experiments. In order to get to this particular configuration, the information presented previously in section 2.4 was used and several iterations tuning the different numerical parameters presented below were performed.

6.1.1 Geometries and mesh

The tubes were modelled by means of two cylindrical shells. Two shells were chosen to represent the tube lay-up since the work from Rabiee [52] depicts that, once more than one layer is used, the results trend to the experimental ones and the number of layers affects then mainly to both the symmetry of the solution's shape and the computational time but not to the studied variables. Each of these two shells represented the mid plane of one half of the laminate each. The dimensions of the geometries are included in Table 6-1. The shells were implemented with 2x2 mm quadrilateral fully integrated (element type 16) multi-layered shell elements. These fully integrated shell elements are based on the Belytschko-Wong-Chiang shell formulation [49]. Four integration points representing each of the composite layers were used thus representing half of the laminate stack. These integration points were oriented according to the laminate design. To activate the laminate theory the LAMSHT flag was activated

in the CONTROL_SHELL card which corrects the assumption of constant shear strain through the shell thickness [49].

The impactor was modelled with a 300x300x25 mm rigid solid box with 10x10x25 solid elements. An overview of the full model can be seen in Figure 6-1.

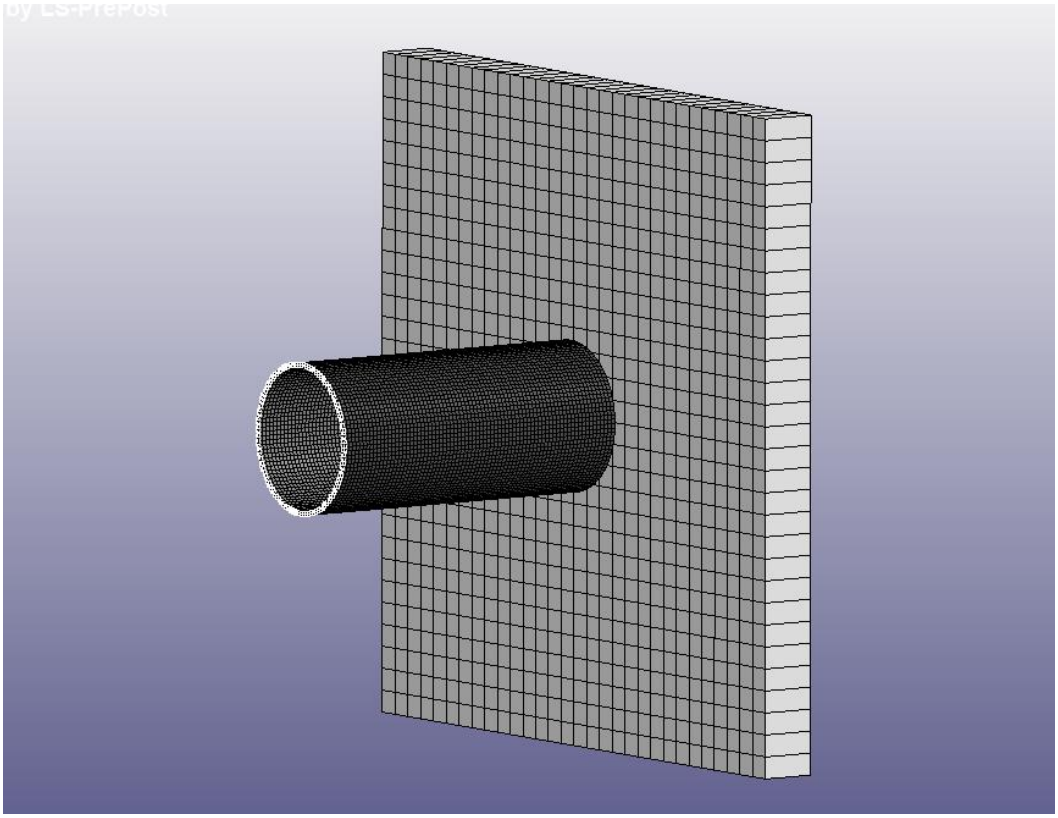

Figure 6-1. FEA model overview.

6.1.1.1 Trigger geometries

The bevel trigger mechanism was modelled by a geometrical simplification to adapt it to the two-shell models. A difference in the shells length was used to represent the chamfer angle characteristic of these triggers, as include in Table 6-1. This is also shown in Figure 6-2. The comparison among the real tube and the model tube is shown in Figure 6-3 and Figure 6-4.

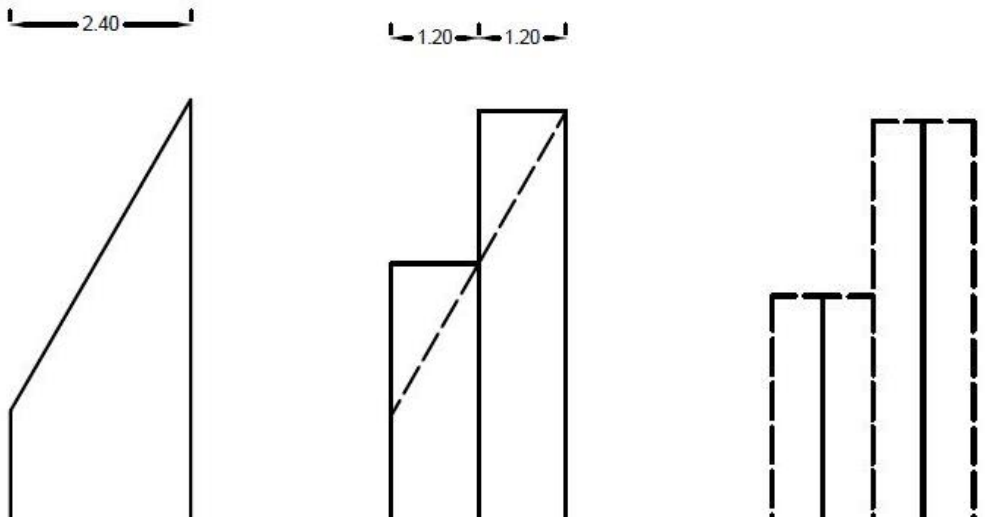

a) b) c)

Figure 6-2. Bevel triggers simplification. Section view of tube's wall. Actual geometry (a), two-laminate simplified geometry (b) and two-shell model simplified geometry (c). Dotted lines represent simplifications.

a) b)

Figure 6-3. B30 specimen (a) and model (b) front views.

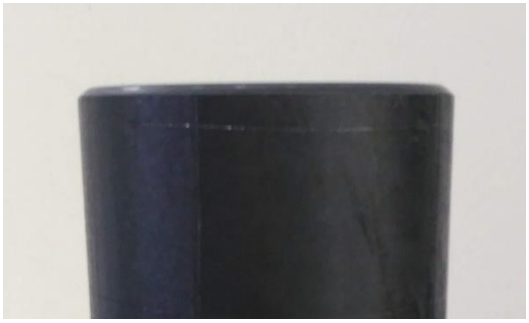

a)

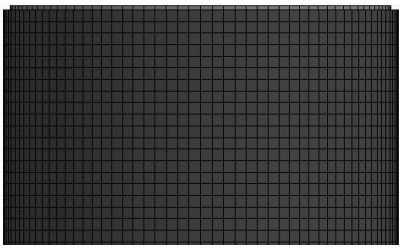

b)

Figure 6-4. B60 specimen (a) and model (b) front views.

Table 6-1. Summary of the initially modelled tube's and trigger's dimensions.

	Inner Shell		Outer Shell		Trigger Geometry	
Model	Diameter (mm)	Length (mm)	Diameter (mm)	Length (mm)	Trigger angle (deg.)	Tips' length (mm)
B60	66.4	150.0	68.8	149.3	60	N/A
B30	66.4	150.0	68.8	147.9	30	N/A
4T60	66.4	150.0	68.8	150.0	60	47.6

There was no need to add any other artificial trigger such as thickness reduction in the elements around the top end as other authors reported [38]. Furthermore, this technique was tested and produced a double slope loading force response due to the early failure of the thinner elements. Then, the simplified geometrical trigger was proved to effectively promote the progressive failure of the tubes.

Regarding the tulip triggers, the tube's cross-section was simplified in the same fashion as shown in Figure 6-2. However, to promote a stable crushing of the tubes, the tips of the tube were slightly forced both inwards and outwards respectively to prevent an only-inwards folding that was obtained otherwise. This was done by means of a 0.5 mm displacement of the tips' top nodes normally to the tube. A detail of the resultant trigger's shape is included in Figure 6-5.

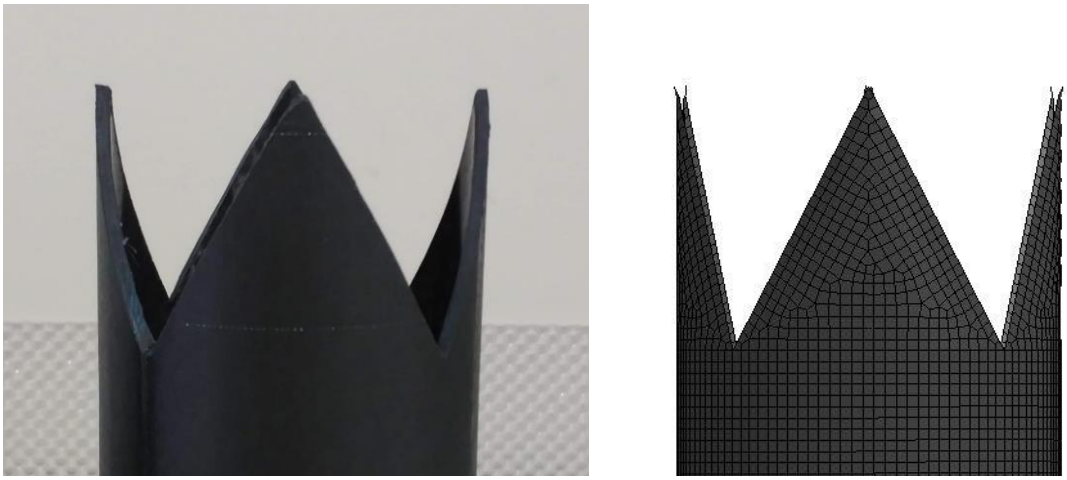

a) b)

Figure 6-5 4T60 specimen (a) and model (b) front views.

6.1.2 Material definitions

The LS-DYNA material model used to represent the CFRP material was the broadly reported (as described in section 2.4) “054/055 enhanced composite damage”. Within this one, the Mat_55 failure criteria was finally used since it represented closely the failure mechanism taking place in the actual samples. MAT_54 was discarded as it showed a progressive fragmentation failure mechanism which differed from the actual mode takin place in the experiment. This material type (55) is based on the Tsai-Wu failure criteria, whereas the Mat_54 implements the Chang-Chang one. These two models differ in the failure criteria for the matrix phase [50]. The governing equations of Tsai-Wu failure model can be found in LS-Dyna user’s manual [50]. The parameters included in this material card which were used to tune the model set-up in order to fit the experimental results are included in Table 6-2. As observed, the model includes the elastic and physic properties of the material as well as several damage and failure values. Material’s strength properties had to be reduced by a 25% from the Datasheet values (Table 3-1) to fit the experimental results in terms of peak load and mean force. This can be justified since, as the curing process was not in autoclave, the resultant properties could differ from datasheet ones. Also, the long and handy process could have introduced defects on the samples. However,

as shown later, this reduction was valid for the three model cases that were compared with the experiments, revealing that this strength reduction actually happened in the samples and was not just a modelling hack. The strains at failure were reduced in the same amount as the strengths since their values were directly calculated from modulus and strength information provided from the datasheet

Regarding the impactor, steel properties and a tuned density to reach the desired mass were used. The mechanical properties were not relevant as it was defined as rigid solid.

Table 6-2. Material model 55 parameters.

Material parameters			Numerical parameters		
Parameter	Value	Description [50]	Parameter	Value	Description [50]
RO (kg/m^3)	1500	Mass density	TFAIL	0.65	Time step size criteria for element deletion
EA (GPa)	119.3	Young's modulus – longitudinal direction	SOFT	0.7	Softening reduction factor for material strength
EB (GPa)	8.2	Young's modulus – transverse direction	FBRT	0	Softening for fibre tensile strength
PRBA	0.01	Poison's ratio ba	CRIT	55	Failure criterion
GAB (GPa)	3.6	Shear modulus, AB			
XC (GPa)	0.8	Longitudinal compressive strength			
XT (GPa)	1.71	Longitudinal tensile strength			
YC (MPa)	150	Transverse compressive strength			
YT (MPa)	40.5	Transverse tensile strength			
DFAILM	0.016	Maximum strain for matrix			
DFAILS	0.021	Maximum tensorial shear strain			
DFAILT	0.014	Maximum strain for fibre tension			
DFAILC	-0.005	Maximum strain for fibre compression			

6.1.3 Contact definitions

Three contact definitions were used in the model. Firstly, a contact between the impactor and the tube was defined using an automatic surface to surface contact law. Impactor's part was defined as master and a shell set involving both tube's shells was defined as slave. The friction factor was fixed to 0.05. This value was tuned to match the mean force results as per the strength reduction technique explained before the peak force was affected too. Also, higher friction values led to higher element distortion around the contact area.

Secondly, an automatic one way automatic surface to surface tie break contact was defined to represent the bonding of the two shells. This enable the model to take into consideration the mode I delamination mechanism. In this case, the friction factor was fixed to 0.23, as found in the work from Schön [53]. This type of contact eliminates the nodes connection when Equation (6-1) is satisfied [49]. Option 8 was set within the contact card making the contact failure to be only stress based. Other Options such as 11 were not considered since they also require material's fracture toughness information which was not available and it was decided not to introduce more unknown variables as with rule 8 the model already showed results' consistency.

$$\left(\frac{|\sigma_n|}{NFLS}\right)^2 + \left(\frac{|\sigma_s|}{SFLS}\right)^2 \geq 1 \qquad \textbf{(6-1)}$$

Where σ_n and σ_s are the normal and shear stresses on the interface and *NFLS* and *SFLS* represent the normal and shear strengths of it.

As in the work from Zhang, the NFLS and SFLS were defined as the material's known interlaminar shear strength, listed in Table 3-1. As mentioned before, material's strengths were reduced by a 25% factor to adjust the load response. However, a reduction of the 50% was applied to the ILS for a fine load adjustment. This can be justified as the delamination taking place in the experiments occurred in the 0º//90º interface which is weaker than the UD interface of the ILS measurements.

To represent the contact of the tube with itself which is a scenario that may occur during the crushing, the general contact algorithm was used. Again, as the only other contact taking place a part from the impactor against tube was the tube self-contact, the friction factor was fixed to 0.23. Table 6-3 summarises the contact algorithms and parameters used.

Table 6-3. Contact definitions and parameters.

Model's contact definitions				
Automatic surface to surface.	Automatic one way surface to surface one way.			General contact
Factor of friction	Factor of friction	NFLS (MPa)	SFLS (MPa)	Factor of friction
0.05	0.23	42.4	42.4	0.23

6.1.4 Loading and boundary conditions

As per testing, impactor's mass was 80 kg with a predefined initial velocity of 5 m/s thus representing the 1 kJ impact test. Specimen's bottom end was allocated fixed boundary conditions to prevent lateral displacements, following also the modelling trends presented in section 2.4. To ensure an axial motion of the impactor, only its movement along the tube's axis was permitted.

6.2 Model validation

The validation of the model represented a challenging stage since, first, the same model should be useful to represent two geometrically different triggers and second, the correlation should cover not only the numerical values but also the macroscopic behaviour of the tubes. This two goals were achieved with the model set up presented above. Results of this validations process are presented down below. The output taken from the model was the force-displacement response. Force pulse was smoothened using a SAE filter @ 1000 Hz which corrected the signal reducing high frequency pulses that drove to high and sharped force values.

Figure 6-6 to Figure 6-8 show the force-displacement responses of the three tested and modelled specimens. Performance results as well as numerical errors are included in Table 6-4.

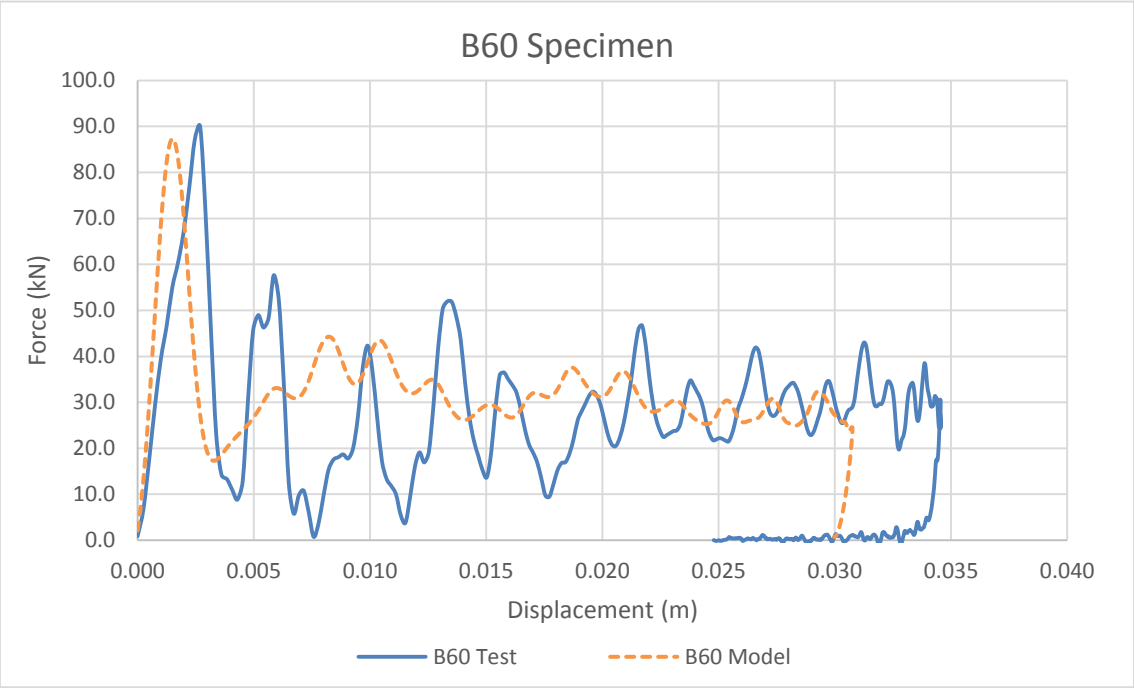

Figure 6-6. B60 specimen. Force-displacement response. Experimental and numerical comparison.

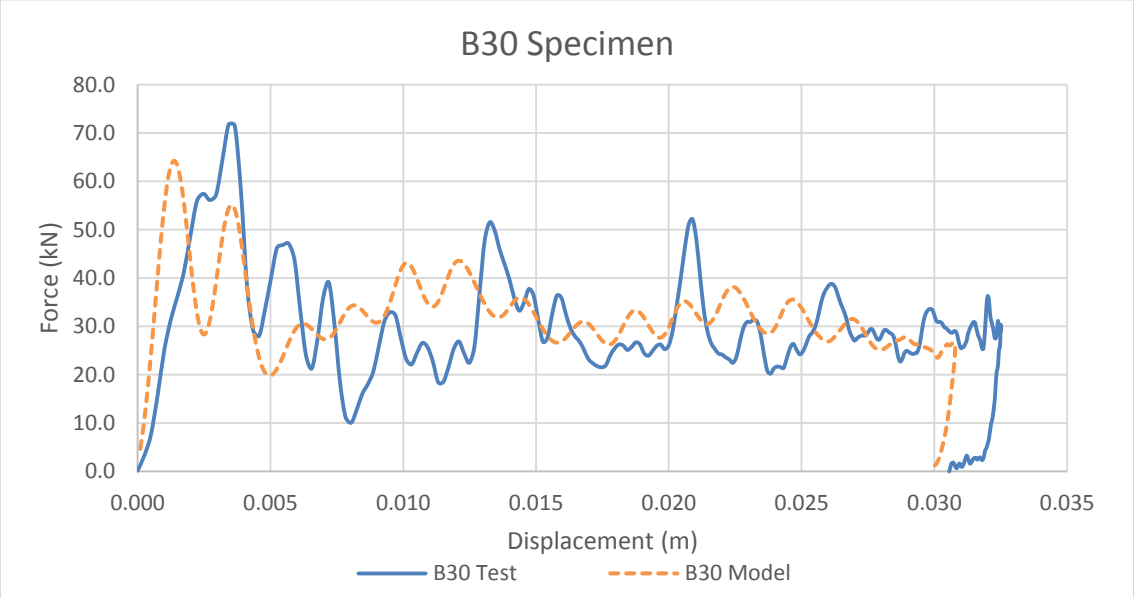

Figure 6-7. B30 specimen. Force-displacement response. Experimental and numerical comparison.

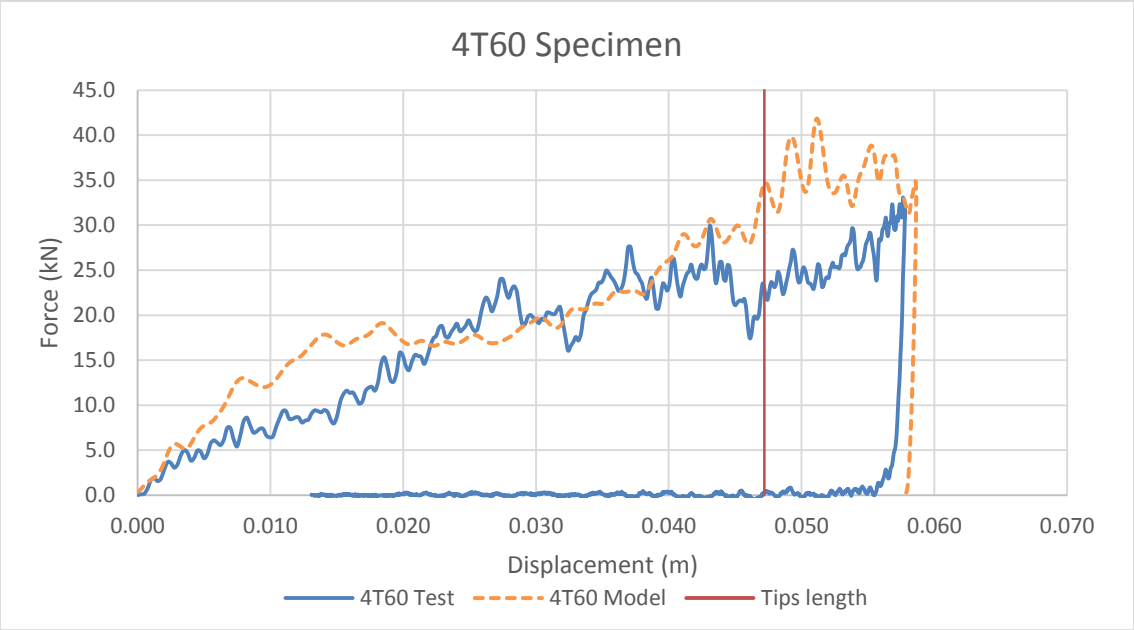

Figure 6-8. 4T60 specimen. Force-displacement response. Experimental and numerical comparison.

Regarding the bevelled tubes, Figure 6-6 and Figure 6-7 show how the simulations underestimate the value of the peak force. By contrast, they overestimate the mean force value, thus producing that all the impact's energy is absorbed within less displacement. Another difference in the responses can be spotted in the depth of the load drops during the stable crushing stage. These deep drops taking place in the experiments can be due to fibre fracture which is not well-achieved in the simulations as explained later on. The double-slope loading response of B30 specimen is due to a time gap in the initial contact of each of the shells against the impactor since the difference in length is greater than in the case of the B60 specimen. Nevertheless, in overall, the response of the simulation showed good correlation as shown in the relative errors included in Table 6-4 and the tubes' failed shapes showed in Figure 6-9 and Figure 6-10. The level of correlation is depicted in the value of the errors collected in Table 6-4 for these tubes. These, except for the CFE, don't go much above the 10%.

Regarding the correlation of the tulip simulations, Figure 6-8 depicts an overestimate in the early stages of the tube's loading which is corrected still during the triggers crushing. Biggest difference can be depicted once the trigger

is consumed and the crushing of the tube's full section starts. Here, the model leads to a higher peak load. At his stage, the slope of both the experiment and the simulation are quite similar, however, experiments' results presents a drop before it which creates a difference in the final peak loads. In fact, simulation's response makes more sense than experimental one since represents the initial constant tube's loading due to the increasing section of the tips, followed by a stable crushing load once the triggers are consumed. Nevertheless, the overall performance is well-represented as can be observed by the match in mean force and displacement, the relative errors included in Table 6-4 which are under the 3% and the visual correlation of the tubes failing mode, shown in Figure 6-11.

Table 6-4. Summary of experimental and numerical results and errors.

Result	F_{max} (kN)	F_m (kN)	d (mm)	SAE (kJ/kg)	CFE (%)	SE (%)
B60 Test	89.9	28.9	34.6	38.0	32.2	22.9
B60 Model	87.3	32.5	30.8	42.7	37.2	20.5
Error (%)	2.9	12.3	11.0	12.3	15.7	10.4
B30 Test	71.8	30.8	32.5	40.1	42.9	21.7
B30 Model	64.2	32.5	30.8	42.7	50.6	20.5
Error (%)	10.5	5.6	5.3	6.3	17.9	5.3
4T60 Test	33.1	17.3	57.8	37.1	52.3	38.5
4T60 Model	33.5	17.1	58.6	36.2	50.9	39.1
Error (%)	1.2	1.5	1.5	2.4	2.6	1.5

As mentioned, not only the values of the performance parameters were important to be matched, but also the behaviour of the tubes. That would ensure that the model represents the same mechanisms as the experiments. As observed in Figure 6-9, Figure 6-10 and Figure 6-11, the tubes effectively failed by a mode I central delamination and certain fracture (represented by the element deletions). Longitudinal cracks leading to petal formation did not visually happen leading to a fully circumferential crack progression. However, petal formation seemed to be prevented by element distortion instead of deletion at the points where this longitudinal cracks should be initiated. Also, the main difference between the

numerical visual results and the experimental ones is the full rolling behaviour of the shells. This did not happen in the experiments in that amount as the bundles also trended to delaminate from each other in mode II creating a lamina bending shape.

a)

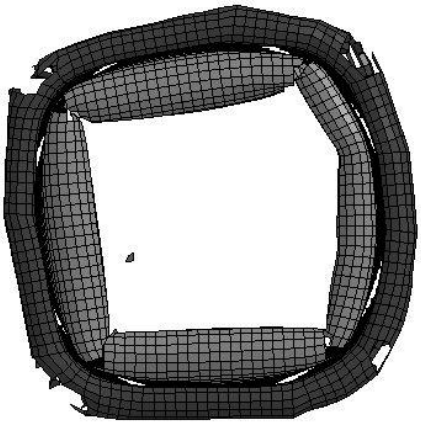

b)

c)

d)

Figure 6-9. B60 specimen. Comparison between macroscopic experimental (top view (a), overview (c)) and numerical results (top view (b), overview (d)).

a)

b)

c)

d)

Figure 6-10. B30 specimen. Comparison between macroscopic experimental (top view (a), overview (c)) and numerical results (top view (b), overview (d)).

a)

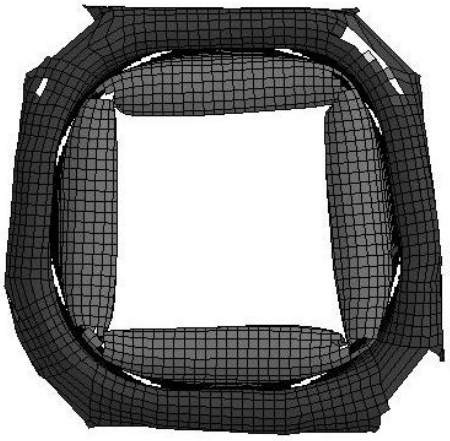

b)

c)

d)

Figure 6-11. 4T60 specimen. Comparison between macroscopic experimental (top view (a), overview (c)) and numerical results (top view (b), overview (d)).

7 PHASE 5 – TRIGGERS' NUMERICAL OPTIMISATION

Once the model was proved to be reliable, it was used to test numerically other designs. These were based on the tested specimens but with modified geometries.

Two different chamfered tubes were modelled and simulated. Since the B30 specimen showed higher SAE than the B60, it was decided to reduce further the chamfer angle until 15º. Also, the 45º chamfered tube was tested as it is widely used and stays in between the 30º and 60º tested specimens. This models were called B15 and B45 respectively.

To investigate further the tulip trigger, two techniques were numerically tested to find the best way to rise up the loading part of the force response thus leading to higher values of mean force. Despite this tube experimentally exhibited a certain drawback in SAE compared to the bevelled tubes, the shape of its response brings a benefit in terms of occupant safety. This idea has been previously discussed in sections 5.3 and 5.4. The first of these explored techniques was to increase the tip's angle from 60º to 90º, for what the model 4T90 was created. The second one was to increase the number of tips from 4 to 6, and was evaluated with the 6T60 model. The aim of these two was to produce a faster and shorter load rising to advance the tube's full-section crushing thus incrementing the overall mean force and also SAE by means of more longitudinal cracks. Finally, a model combining these two solutions was tested to see the interaction. This model was called 6T90.

All these models were created with the same geometrical simplifications and solver set up described in section 6.1. Table 7-1 summarises the dimensions of the modelled geometries.

Table 7-1. Summary of redesigned tube's and trigger's dimensions.

	Inner Shell		Outer Shell		Trigger Geometry	
Model	Diameter (mm)	Length (mm)	Diameter (mm)	Length (mm)	Trigger angle (deg.)	Tips' length (mm)
B15	66.4	150.0	68.8	145.5	15	N/A
B45	66.4	150.0	68.8	148.8	45	N/A
4T90	66.4	150.0	68.8	150.0	90	27.5
6T60	66.4	150.0	68.8	150.0	60	31.8
6T90	66.4	150.0	68.8	150.0	90	18.3

7.1 Bevel Triggered Designs

Figure 7-1 gives a detail of the further investigated bevel triggers.

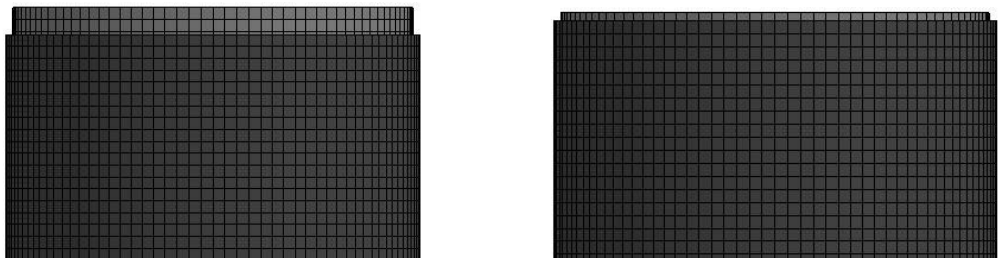

a) b)

Figure 7-1. Triggers' detail of the B15 (a) and B45 (b) models.

Figure 7-2 includes the force-displacement responses of these two chamfered tubes. The B15's curve depicts how the initial contact lagging effect due to the difference in the shells length observed already for the B30 specimen is accentuated. Also, as the angle gets smaller, the trigger gets longer, leading to a shift in the point in which the stable crushing starts thus producing a lower mean force. This can be observed comparing the maximum displacement of the B45 and the B15 specimens. B15's displacement is greater, revealing a smaller resultant mean force. Figure 7-3 collects the visual results of the tubes crushing. These are very similar to the ones showed previously in section 6.2 being the B45 failure the most rounded and symmetrical bevelled result so far.

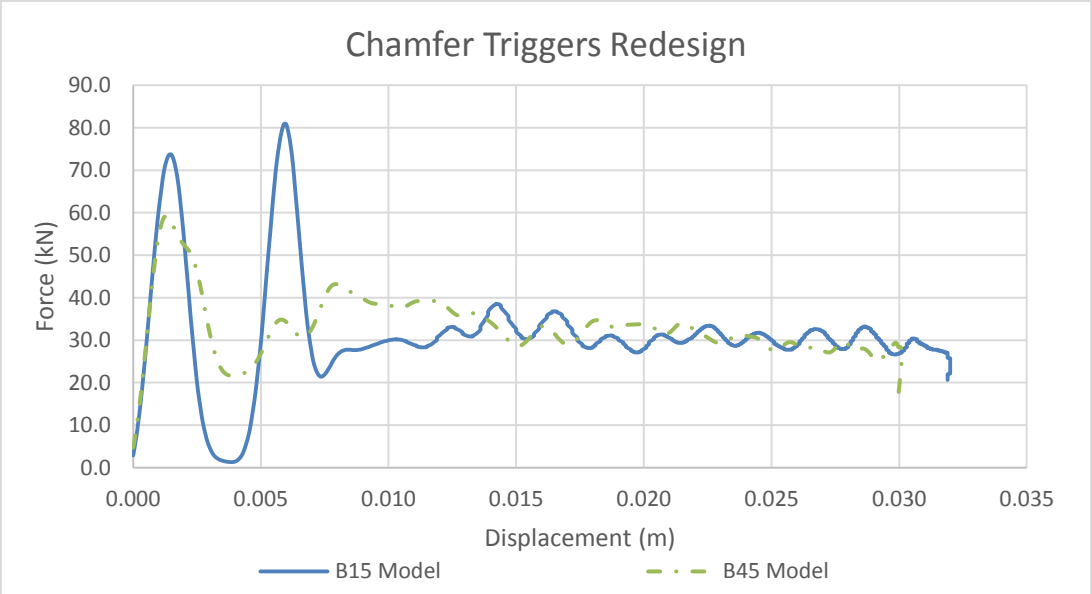

Figure 7-2. Force-displacement response of the redesigned chamfered tubes.

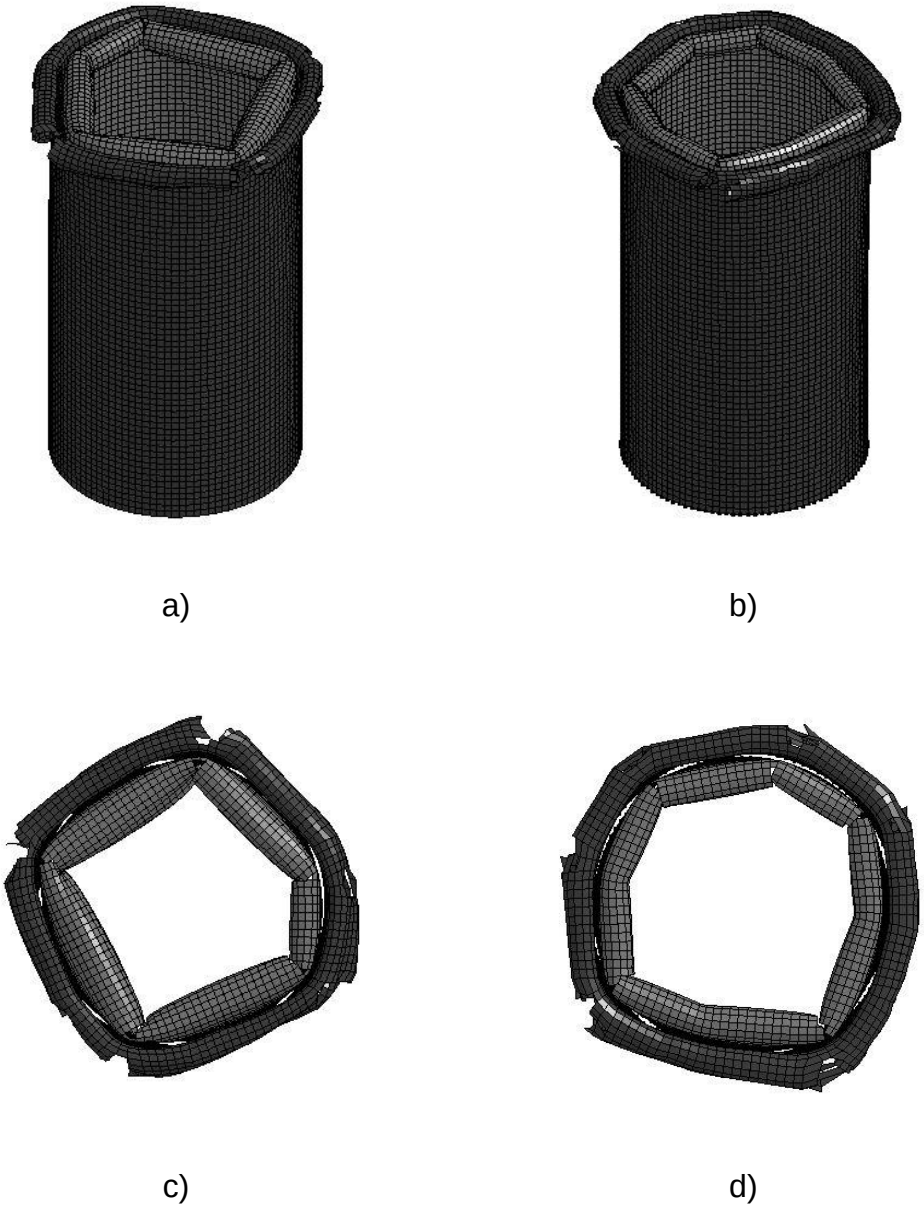

Figure 7-3. Macroscopic results of B15 (overview (a) and top view (c)) and B45 (overview (b) and top view (d)) models.

In Figure 7-4 and Table 7-2, all the chamfered tubes modelled so far are analysed. The trend in the force-displacement curves is quite stable, and the biggest difference appears in the peak force duration and shape produced by the mentioned initial contact gap effect. Results are quite sable in crushing force,

revealing that all the tubes failed in a similar and controlled manner. Further conclusions are better analysed by means of the bar charts shown later.

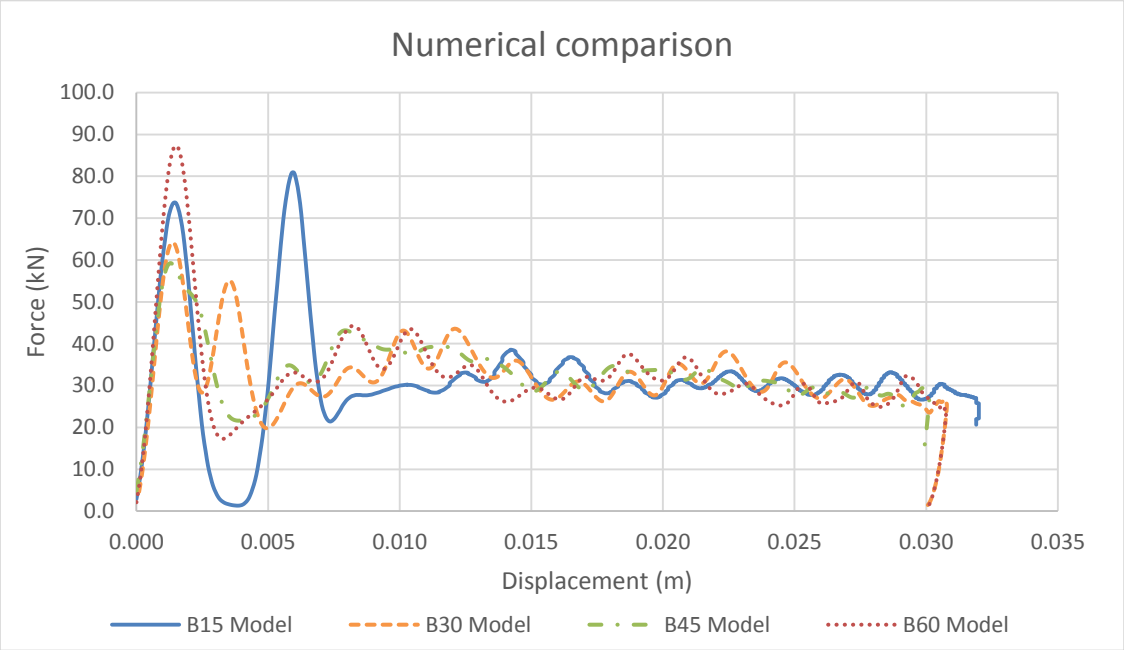

Figure 7-4. Bevel triggers' numerical comparison.

Table 7-2. Bevel trigger model's performance results.

Trigger	F_{max} (kN)	F_m (kN)	d (mm)	SAE (kJ/kg)	CFE (%)	CE (%)
B15 Model	80.8	31.3	32.0	41.0	38.7	21.3
B30 Model	64.2	32.5	30.8	42.7	50.6	20.5
B45 Model	59.3	33.2	30.1	43.6	56.0	20.1
B60 Model	87.3	32.5	30.8	42.7	37.2	20.5

Table 7-2 together with Figure 7-5 gives a good baseline for comparing the different analysed models. On them, first it is clear that all the mean forces are very similar, what produces also similar results in maximum displacement. However, already in these two parameters, model B45 presents slightly improved results compared to B30, which was chosen as best specimen in the experimental stage. Further comparisons depict how both SAE and CFE present higher results for mid values of chamfer angle, thus being the lowest results for the extreme angle values. This effect occurs in opposite trend for the maximum force results, as the highest and lowest angles present the highest values of peak

load. Thus, results point towards B45 as optimal solution within the bevel type trigger. This model exhibited the highest SAE and CFE as well as the lowest peak load, with the rest of parameters very close to the other models. Compared to the B30 model (chosen as best specimen in the experimental stage), B45 presented an improvement in SAE of the 2.1% as well as a reduction in peak force of the 7.6%.

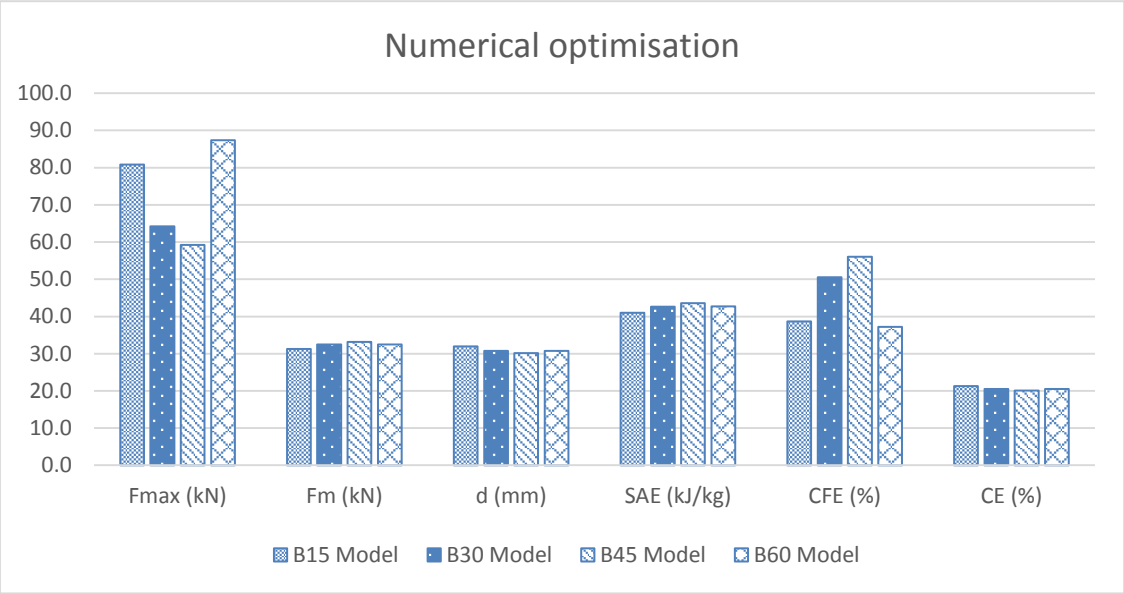

Figure 7-5. Performance comparison of the bevel trigger models.

7.2 Tulip Triggers Designs

Figure 7-6 gives a detail of the further investigated bevel triggers.

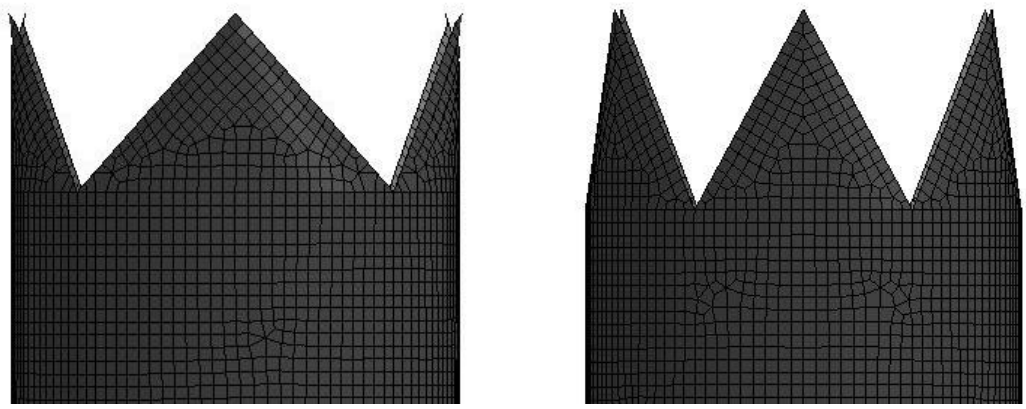

a) b)

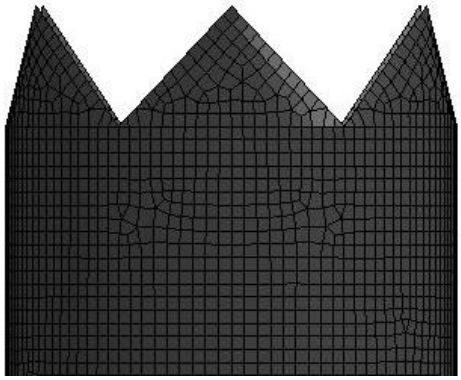

c)

Figure 7-6. Triggers' detail of the 4T90 (a), 6T60 (b), and 6T90 (c) models.

Figure 7-7 shows the tips' angle effect, comparing the 4T60 and 4T90 results. The force-displacement responses clearly show that the effect is positive for energy absorption purposes, and the increase in angle is translated in a faster (stiffer) loading stage. Furthermore, as the tips get wider, they get also shorter, what anticipates the tube's full-section crushing leading to a smaller final displacement. These two effects were the ones aimed to enhance this tubes' performance. Therefore, it can be said that the angle's increasing effectively improved the performance of tulip triggered tubes. This is numerically justified with the parameters' results collected in Table 7-3. Looking at the tube's macroscopic behaviour of Figure 7-9, however, it has to be said that the crushing looks less stable. In fact, one of the outer tips tears a part and folds inwards so results might be affected by this difference in the progressive crushing.

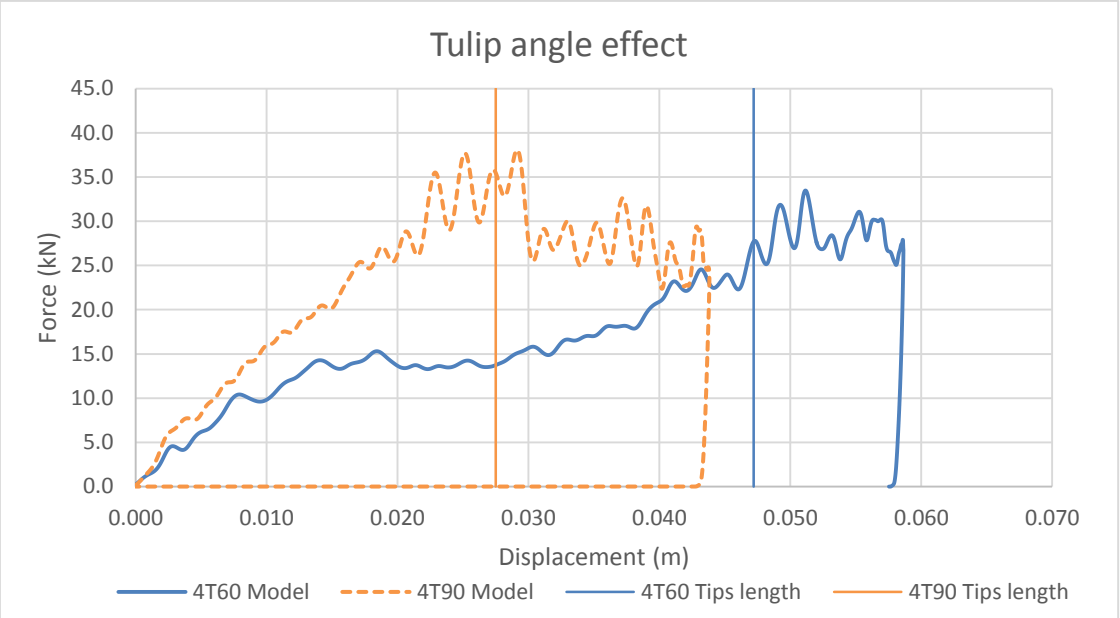

Figure 7-7. Force-displacement responses of 4T60 and 4T90 models.

On the other hand, Figure 7-7 shows the effect of the number of tips in the force-displacement response of tulip tubes. The improvement is clear and can be observed in the shorter displacement, which is translated in a higher mean force. The curve depicts that there is small effect on the loading stage. Thus, the impact of the number of tips is reflected mainly in the anticipation of the full-tube's section crushing. Despite this effect is positive for the crashworthiness behaviour of the tube, it does not appear accompanied with a faster (stiffer) loading stage, thus making this technique less efficient than the increase in the tips' angle. Also, Figure 7-9 shows how visually the tube failed in a very stable way, showing in fact the most rounded and symmetrical post-failure section so far. This can reveal that increasing the number of tips produces an improvement in the stability of the failure.

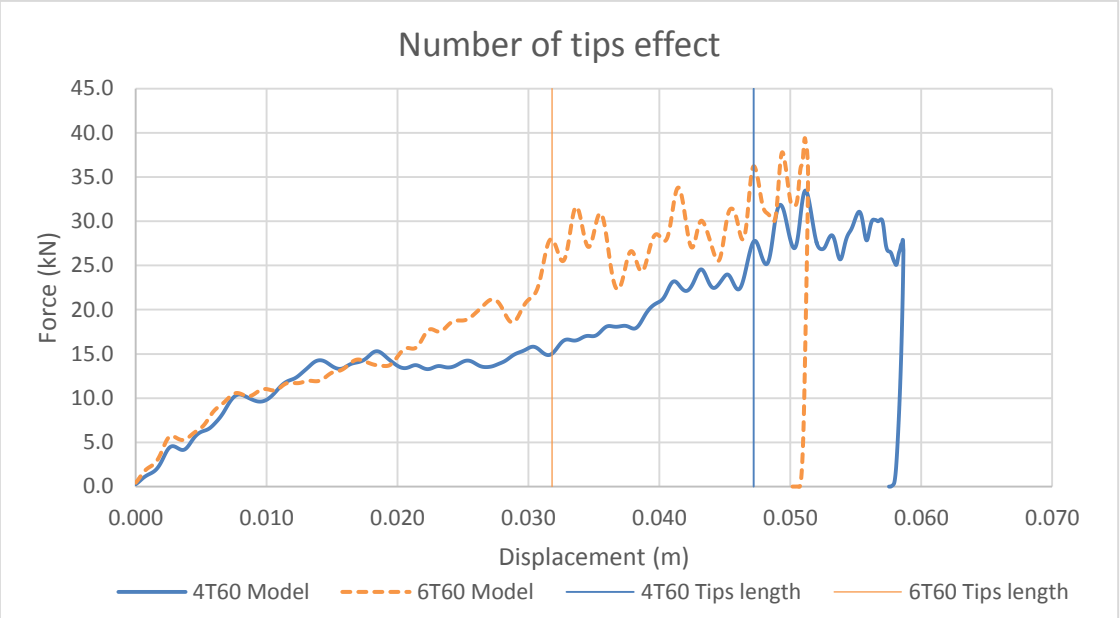

Figure 7-8. Force-displacement responses of 4T60 and 6T60 models.

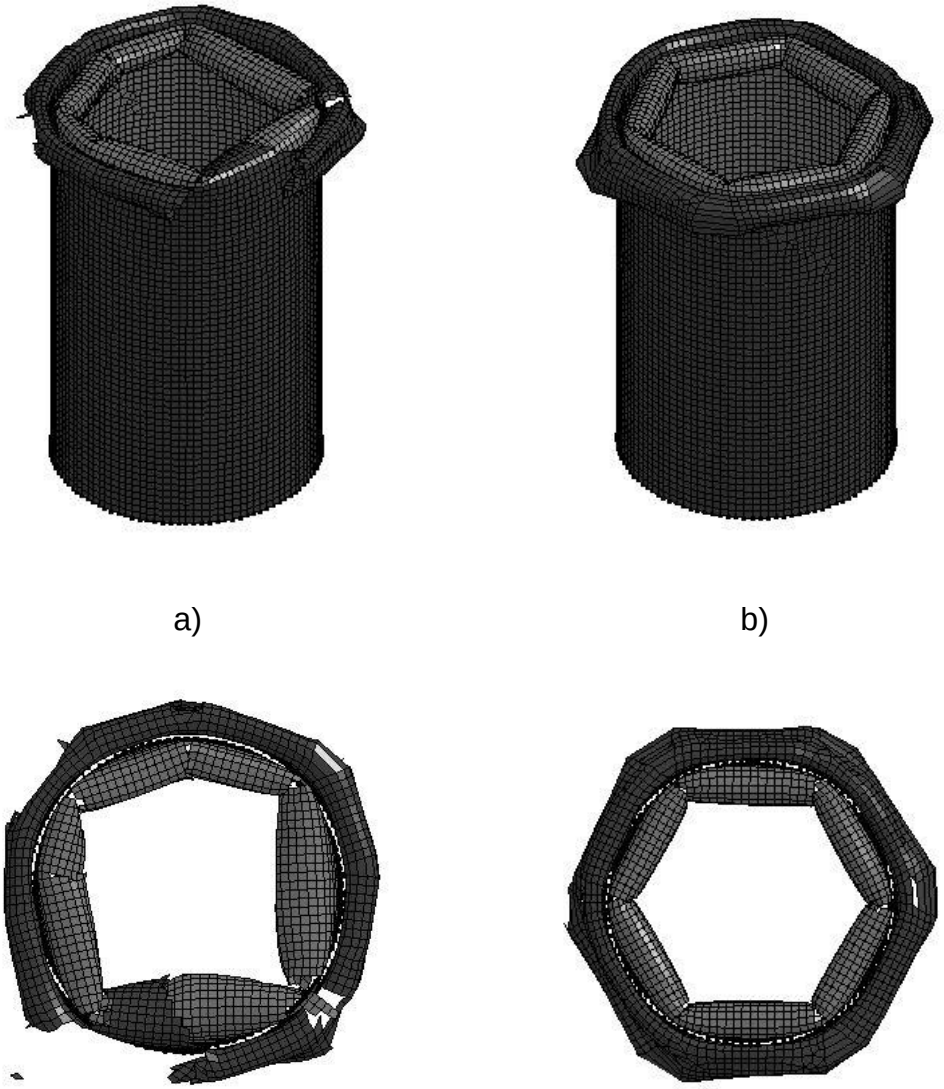

a) b)

c) d)

Figure 7-9. Macroscopic results of 4T90 (overview (a) and top view (c)) and 6T60 (overview (b) and top view (d)) models.

Figure 7-10 compares the redesigned tulip triggers and Table 7-3 quantifies this comparison. Here, performance results as well as the relative difference compared to the 4T60 baseline model are included. First thing to highlight is that since the 4T90 design involved a certain failure instability, its results might be affected and were not taken as comparable for producing a not fully equal failure mode. As mentioned before and observed in the results, one more specimen was modelled to assess the effect of combining both a wider angle and a bigger number of tips. Force response is included in Figure 7-11, where all the tulip models are compared together.

The results show that enlarging the angle produces higher benefits than increasing the number of tips in the tube. The impact produced in mean force by the angle effect was quantified in a 22%. For that, 6T60 and 6T90 models were compared as 4T90 was not fully comparable. On the other hand, comparing the 4T60 and 6T60 models, changing the number of tips presented a difference of a 14%. SAE seemed to be only sensitive to the tips' angle, presenting an increase from the 6T60 model to the 6T90 of the 8.5%.

In overall, numerical results of Table 7-3, show that the 6T90 configuration effectively produces an improvement compared to all previous tulip tubes (regardless of the unstable 4T90). This leads to a SAE of 39.4 kJ/kg, close the results exhibited from the bevelled triggers (42.5 kJ/kg in average) but bringing the soft loading benefit and producing an improvement of the 8.8% compared to the 4T60 baseline tulip model. The results from the 6T90 model confirms that the effect of increasing the number of tips affects mainly to the full-section tube crushing starting point and not to the loading stage slope. Thus, the improvement from the 4T90 model to the 6T90 is slight, but exists. Finally, looking at its failure results (Figure 7-12), it is confirmed that increasing the number of tips, the failure becomes more stable. While 4T90 model showed certain instability leading to a tearing of one of the tips, 6T90 presented a rounded and symmetrical crushed shape. Thus, this model enable to see the benefit effect of 90º tulip when the crushing is stable and then results are reliable and comparable.

This model, 6T90, presented the most stable results with improvements from the 4T60 baseline in mean force, maximum displacement, SAE and CFE. Thus, despite not bringing the best SAE value (4T90 was higher), it brought the best stable and reliable results within the tulip models.

Table 7-3. Tulip trigger model's performance results.

Trigger	F_{max} (kN)	F_m (kN)	d (mm)	SAE (kJ/kg)	CFE (%)	CE (%)
4T60 Model	33.5	17.1	58.6	36.2	50.9	39.1
4T90 Model	38.1	22.8	43.8	42.8	59.9	29.2
Diff. (%)	13.7	33.8	25.3	18.2	17.7	25.3
6T60 Model	39.4	19.5	51.4	36.3	49.4	34.2
Diff. (%)	17.7	14.2	12.4	0.3	3.0	12.4
6T90 Model	37.1	23.8	42.0	39.4	64.1	28.0
Diff. (%)	11.0	39.6	28.4	8.8	25.8	28.4

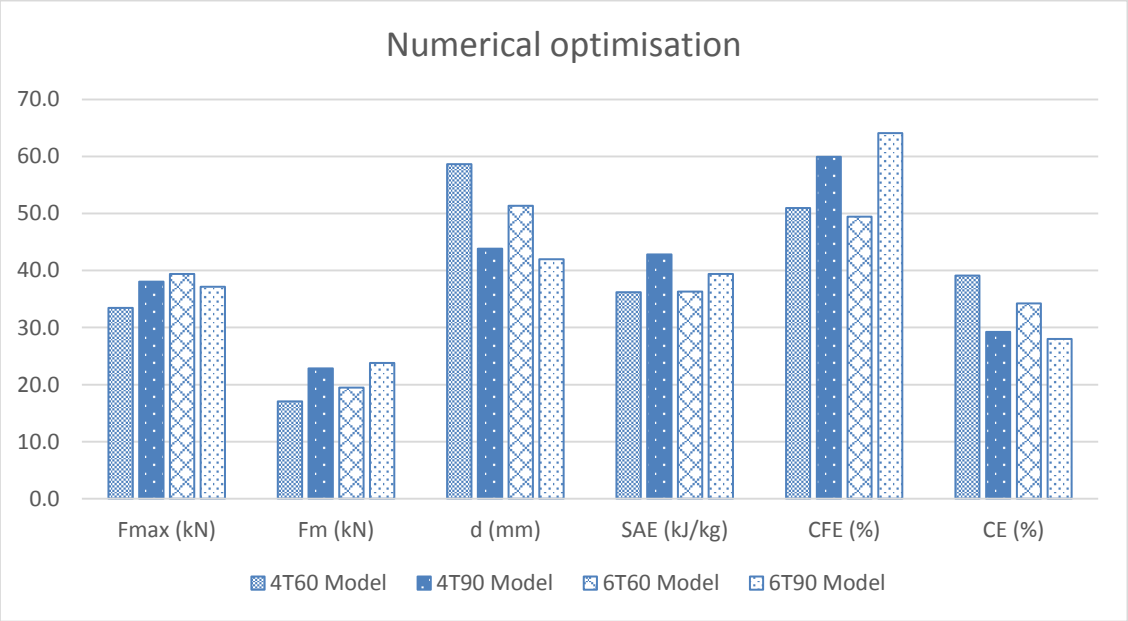

Figure 7-10. Performance comparison of the bevel trigger models.

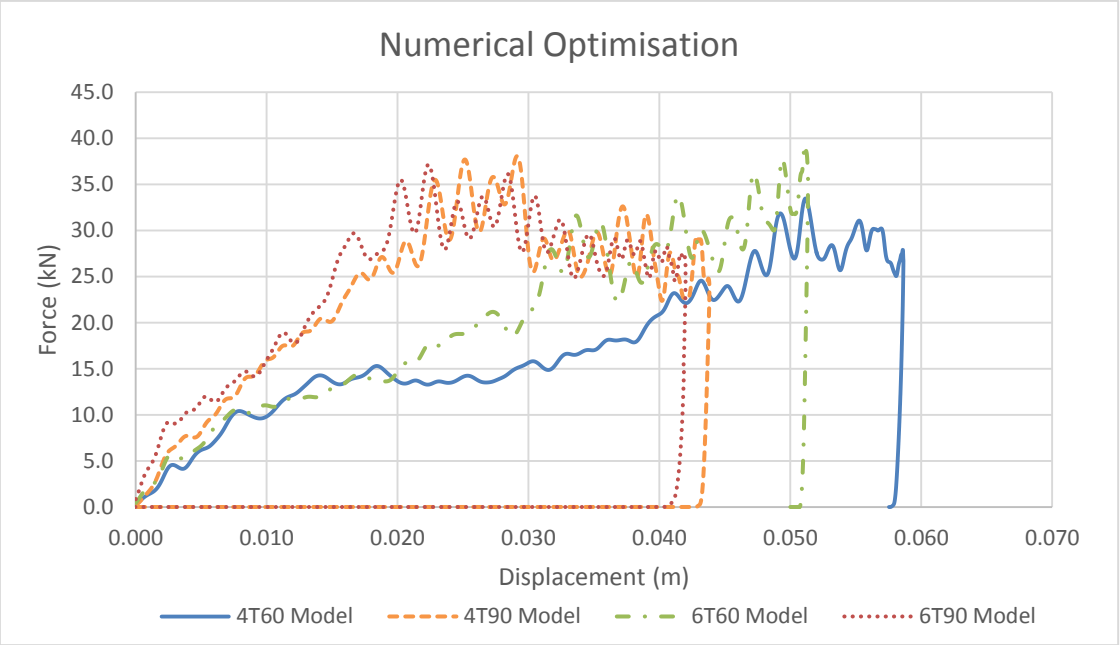

Figure 7-11. Bevel triggers' numerical comparison.

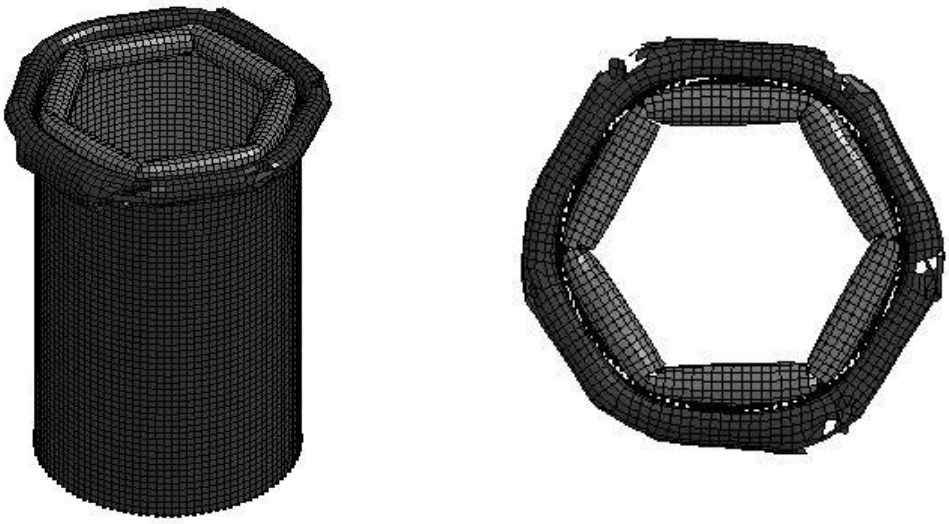

a) b)

Figure 7-12. Macroscopic results of 6T90 model (overview (a) and top view (b)).

7.3 Overall Numerical Comparison

Table 7-4 collects all the numerical results combining both the bevel and the tulip triggered models.

Table 7-4. Overall numerical results comparison.

Trigger	F_{max} (kN)	F_m (kN)	d (mm)	SAE (kJ/kg)	CFE (%)	CE (%)
B15 Model	80.8	31.3	32.0	41.0	38.7	21.3
B30 Model	64.2	32.5	30.8	42.7	50.6	20.5
B45 Model	59.3	33.2	30.1	43.6	56.0	20.1
B60 Model	87.3	32.5	30.8	42.7	37.2	20.5
Average	72.9	32.4	30.9	42.5	45.6	20.6
4T60 Model	33.5	17.1	58.6	36.2	50.9	39.1
4T90 Model	38.1	22.8	43.8	42.8	59.9	29.2
6T60 Model	39.4	19.5	51.4	36.3	49.4	34.2
6T90 Model	37.1	23.8	42.0	39.4	64.1	28.0
Average	37.0	20.8	49.0	38.7	56.1	32.6

These results, together with Figure 7-13 gives an overview of the main differences between the bevel and tulip type triggers models. Results show how, in average, bevelled tubes produced peak loads almost double in value compared to tulip type tubes. This produced that, despite all crushing forces were similar, tulip tubes produced mean forces that in average represented a 35.8% decrease when compared to the ones of bevel models. This also produced remarkably higher values of displacement for the tulip ended tubes. CFE appears as similar for both trigger types, showing however that tulip tubes drive to higher values of this parameter, as in the case of CE. And last but not least, SAE results show that bevel tubes produce higher results in all cases. With a mean difference around 6 kJ/kg.

Finally, Figure 7-14 includes all the force-displacement responses obtained in the redesigning stage. And Figure 7-15 compares the two best designs found for both bevel and tulip triggers.

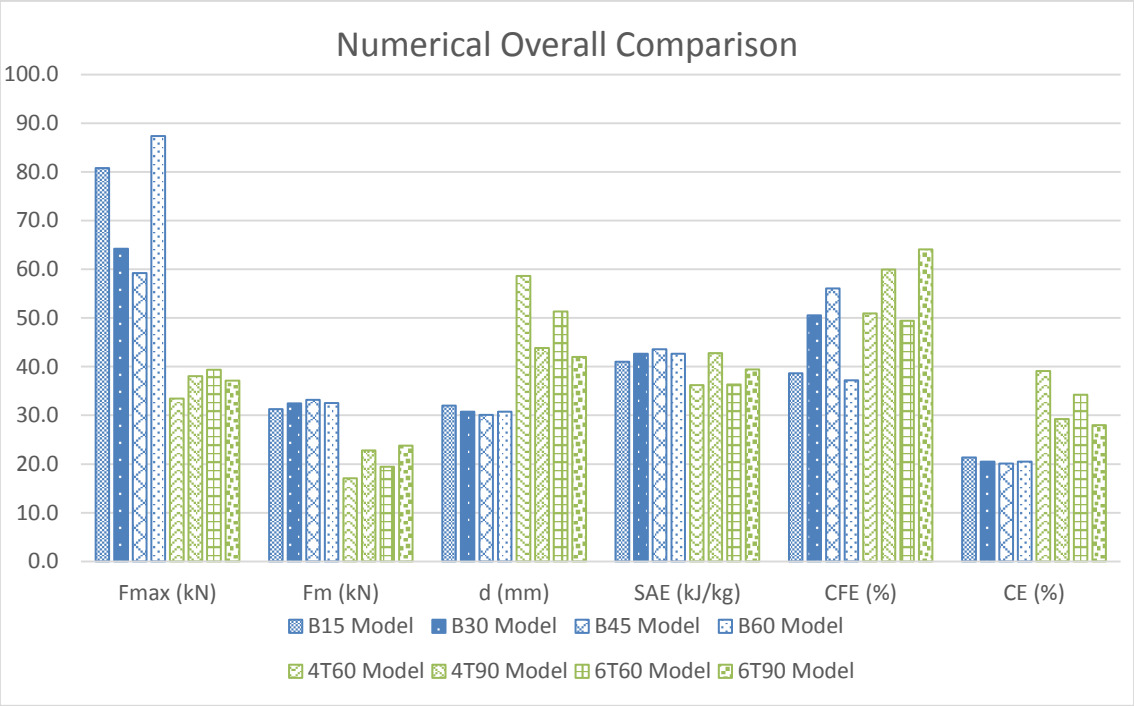

Figure 7-13. Overall numerical results comparison.

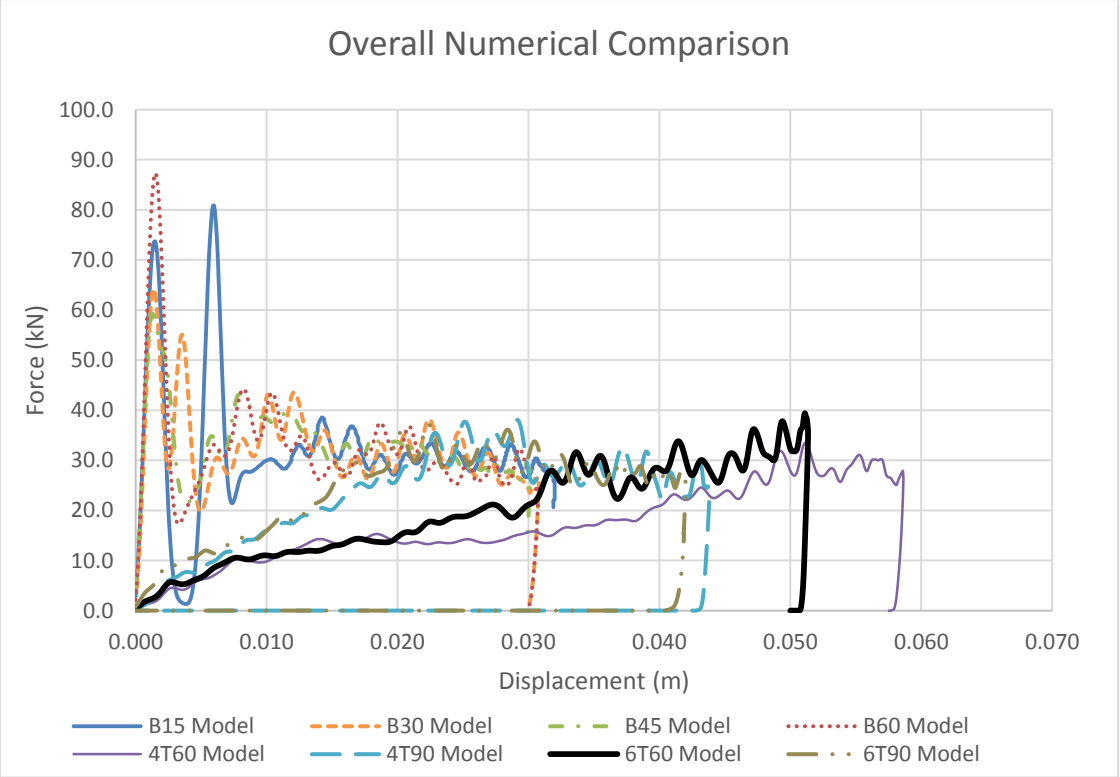

Figure 7-14. Overall numerical comparison.

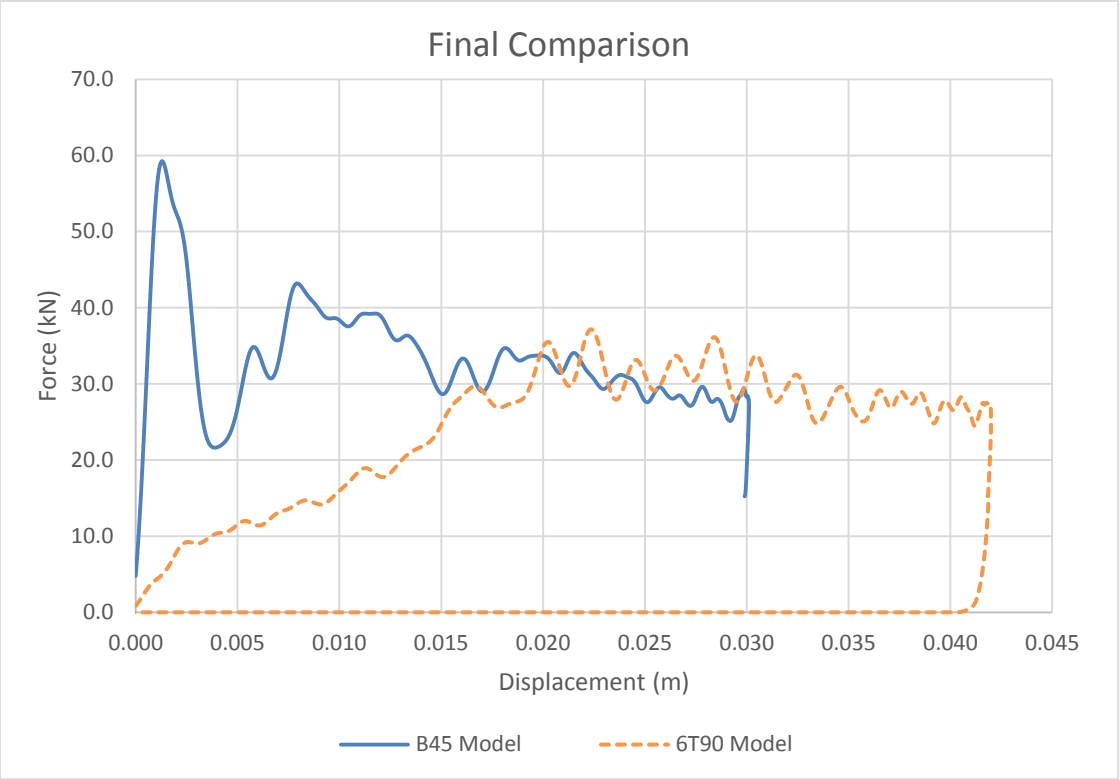

Figure 7-15. Final comparison of the best bevel and tulip triggers found.

8 CONCLUSIONS AND RECOMENDATIONS

The literature review and research stage of the project revealed that importance of trigger mechanisms within the axial crushing of composite energy absorbers is well recognised. However, their presence is sometimes just a means to promote structure's progressive failure and they are not considered as a chance to enhance component's performance. It was shown how bevel triggers are widely used, and that tulip triggers can prevent the structures to produce a sharped and hazardous initial peak load. Through research, it was also observed that for the numerical analysis of axial crushing composite components, LS-DYNA appeared as the most used software.

CFRP tubes were manufactured by means of a hand lay-up process to perform a bevel and tulip triggers characterisation. Then, tubes were trimmed and different trigger's geometries were mechanised in three different specimens. Manufacturing process revealed the complexity and easiness of failure to occur when manufacturing CFRP tubular components by means of these methods.

The experimental phase revealed that the drop tower facility is effectively valid to obtain the force-displacement response of energy absorbers. Specimens failed in a stable and progressive manner, as expected due to its triggered design. The three tubes exhibited a brittle fracture mode, combining both lamina bending certain fragmentation (as well as several bundle failure mechanisms). Within the bevel tubes, chamfer at 30º presented the best results in terms of maximum SAE, mean force and minimum peak load. The tulip specimen presented lower SAE values due to the less amount of failure mechanisms involved during its crushing. However, its force pulse brings the feature of avoiding the hard initial peak load.

Experimental results were used to validate a dynamic FEA model which was set up in LS-DYNA. The model showed good correlation with the experimental results. Showing errors around the 10% for bevel specimens and 2% for tulip type tubes. This difference can be due to the trigger geometrical simplification that the two-shell model involved for the bevel tubes. However, these simplifications had less effect of the tulip specimens. The macroscopic behaviour of the tubes

showed a progressive splaying without large petals formation that produced a rolling motion both inwards and outwards of the walls. This behaviour, despite not being fully equal to the one taking place in the actual specimens, produced force pulses that correlated well with the experimental results in terms of maximum force, crushing load and maximum displacement.

Several models were further developed for a wider analysis of both triggers. Within the bevel tubes, B45 model (chamfer at 45º) exhibited the best results, driving to the highest values of SAE and mean force, as well as the lowest (and therefore safest) maximum force. CFE presented also a maximum value for this design and CE appeared as almost constant with the chamfer angle.

Two techniques were analysed to enhance the performance of the tulip ended tubes. Among them, increasing the tips' angle appeared to be more efficient to improve the mean force than increasing the number of tips. From the 4T60 baseline model they produced an improvement of the 25.4% and 14.2% respectively. Changing the angle was proved to have effect in both the slope of the loading stage of the force response, and bringing forward the stable crushing load starting point. However, it produced a less stable trigger failure. By contrast, increasing the number of tips produced only an effect on the starting point of the crushing force. Nevertheless, this technique presented the most symmetrical and controlled crushing, and therefore it was decided to use it in combination with the angle changing solution. Best results in tulip triggers were achieved by this model (6T90) that involved an increase in both the trigger angle and a number of tips, driving to a final SAE of 39.4 kJ/kg that represented an enhancement from the 4T60 model of 8.8%. Nonetheless, SAE values of this optimised tulip tube, in spite of the fact of reducing the initial high peak load, still resulted slightly below the bevel triggered tubes.

Therefore, the conclusion exclusively in terms of energy and weight optimisation, is that bevel triggered tubes were proved to perform better than tulip type ones. Within this ones, chamfer at 45º showed the best results with a SAE of 43.6 kJ/kg.

However, the force response of the tulip ended tubes presented a crucial benefit for occupant safety purposes, with a SAE slightly reduced (8.9%). Also, their

initial constant rising slope, could be a requirement to meet the overall structural impact response. Within these tubes, triggers with 6 tips at 90º produced the best stable results in terms of SAE. Therefore, if the difference in SAE is accepted, the tulip trigger should be chosen as drives to safer force responses.

Finally, the use of one trigger or the other could also depend on the structure's application and requirements, as it has been proved that trigger mechanisms can be used to tailor the overall response of the energy absorption component.

9 FUTURE WORK

This section covers all the topics and tasks related to the project that either for time, resources or availability constrains could not be covered by present work but represent an outstanding range of ways to complete or supplement to this work.

- Due to time constrains it was no possible to manufacture and test the redesigned specimens. It would be very valuable to perform physical test on the finally selected redesigned samples to prove their actual improvements.
- Only two types of triggers were analysed during the project. It would be interesting to perform a further analysis and model's validation in some of the other triggers that were presented in section 2.3.1.
- Both triggers experimental characterisation and model's validation were perform under the 5m/s test conditions. To complete a wider analyses, tests at different velocities should be performed to assess the triggers behaviour and possible strain rate effects.
- Characterising the triggers behaviour in components manufactured by other more automated techniques such as filament winding would be interesting as it will involve industry-oriented results.
- Finally, a try an error material properties adjustment was perform to set up de FEA model. To be able to introduce the material properties of the exact same tubes, material testing is advised for future projects as will clear one of the unknowns of the model.

REFERENCES

1. Mamalis AG., Johnson W. Crashworthiness of Vehicles. London: Mechanical Engineering Publications Limited; 1978.

2. Seiffert U., Wech L. Automotive Safety Handbook. Second Edi. Warrendale, Pa: SAE International; 2007.

3. United Nations. United Nations Decade of Action for Road Safety 2011-2020. 2009. Available at: http://www.un.org/en/roadsafety/ (Accessed: 28 June 2016)

4. Mamalis AG., Manolakos DE., Demosthenous GA., Ioannidis MB. Crashworthiness of Composite Thin-Walled Structural Components. First Edit. Lancaster: Technomic Publishing CO., Inc.; 1998.

5. Barbero EJ. Introduction to Composite Materials Design. Second Edi. Boca Raton, Fl: CRC Press; 2011.

6. Hosseini SM., Shariati M. Experimental analysis of energy absorption capability of thin-walled composite cylindrical shells by quasi-static axial crushing test. Thin-Walled Structures. Elsevier Ltd; 2018; 125(January): 259–268. Available at: DOI:10.1016/j.tws.2018.01.026

7. Chiu LNS., Falzon BG., Boman R., Chen B., Yan W. Finite element modelling of composite structures under crushing load Finite element modelling of composite structures under crushing load. 2015; 131: 215–228. Available at: DOI:10.1016/j.compstruct.2015.05.008

8. Yan L., Chouw N. Crashworthiness characteristics of flax fibre reinforced epoxy tubes for energy absorption application. Materials and Design. 2013; 51: 629–640. Available at: DOI:10.1016/j.matdes.2013.04.014

9. Abrate S. Impact on composite structures. Cambridge: Cambridge University Press; 1998.

10. O'Rourke BP. The uses of composite materials in the design and manufacture of Formula 1 racing cars. ARCHIVE: Proceedings of the

Institution of Mechanical Engineers, Part D: Journal of Automobile Engineering 1989-1996 (vols 203-210). 1990; 204(14): 41–48. Available at: DOI:10.1243/PIME_PROC_1990_204_131_02

11. Rabiee A., Ghasemnejad H. Progressive Crushing of Polymer Matrix Composite Tubular Structures: Review. Open Journal of Composite Materials. 2017; 07(01): 14–48. Available at: DOI:10.4236/ojcm.2017.71002

12. Hull D. A Unified Approach to Progressive Crushing of Fiber-Reinforced Composite Tubes. Composites Science and Technology. 1991; 40(4): 377–421. Available at: DOI:10.1016/0266-3538(91)90031-J

13. Atthapreyangkul A., Gangadhara Prusty B. Experimental and numerical analysis on the geometrical parameters towards the maximum SEA of CFRP components. Composite Structures. Elsevier Ltd; 2017; 164: 229–236. Available at: DOI:10.1016/j.compstruct.2016.12.078

14. Mallick PK. Materials, Design and Manufacturing for Lightweight Vehicles. Woodhead Publishing Ltd; 2010.

15. Brown J. ‘Engineering Aspects of the Human Victim in Aircraft Crashes’. [Lecture notes] Structural Aspects of Crashworthiness. MSc Advanced Lightweight Structures and Impact. Cranfield University; 2018.

16. Sivagurunathan R., Lau Tze Way S., Sivagurunathan L., Yaakob MY. The Effects of Triggering Mechanisms on the Energy Absorption Capability of Circular Jute/Epoxy Composite Tubes under Quasi-Static Axial Loading. Applied Composite Materials. Applied Composite Materials; 2018; : 1–17. Available at: DOI:10.1007/s10443-018-9673-5

17. Bisagni C., Di Pietro G., Fraschini L., Terletti D. Progressive crushing of fiber-reinforced composite structural components of a Formula One racing car. Composite Structures. 2005; 68(4): 491–503. Available at: DOI:10.1016/j.compstruct.2004.04.015

18. Baroutaji A., Sajjia M., Olabi A. On the crashworthiness performance of

thin-walled energy absorbers : Recent advances and future developments. Thin Walled Structures. Elsevier Ltd; 2017; 118(April): 137–163. Available at: DOI:10.1016/j.tws.2017.05.018

19. Tarlochan F., Samer F., Hamouda AMS., Ramesh S., Khalid K. Design of thin wall structures for energy absorption applications : Enhancement of crashworthiness due to axial and oblique impact forces. Thin Walled Structures. Elsevier; 2013; 71: 7–17. Available at: DOI:10.1016/j.tws.2013.04.003

20. Salehghaffari S., Tajdari M., Panahi M., Mokhtarnezhad F. Attempts to improve energy absorption characteristics of circular metal tubes subjected to axial loading. Thin Walled Structures. Elsevier; 2010; 48(6): 379–390. Available at: DOI:10.1016/j.tws.2010.01.012

21. Wang J., Zhang Y., He N., Wang CH. Crashworthiness behavior of Koch fractal structures. Materials and Design. Elsevier Ltd; 2018; 144: 229–244. Available at: DOI:10.1016/j.matdes.2018.02.035

22. Hesse SH., Lukaszewicz DHJA., Duddeck F. A method to reduce design complexity of automotive composite structures with respect to crashworthiness. Composite Structures. Elsevier Ltd; 2015; 129: 236–249. Available at: DOI:10.1016/j.compstruct.2015.02.086

23. Lau STW., Said MR., Yuhazri M. On the effect of geometrical designs and failure modes in composite axial crushing : A literature review. Composite Structures. Elsevier Ltd; 2012; 94(3): 803–812. Available at: DOI:10.1016/j.compstruct.2011.09.013

24. Farley GL., Jones RM. Crushing Characteristics of Continuous Fiber-Reinforced Composite Tubes. Journal of Composite Materials. 1992; 26(1): 37–50. Available at: DOI:10.1177/002199839202600103

25. Farley GL. Energy Absorption of Composite Materials. Journal of Composite Materials. 1983; 17(May): 267–279. Available at: DOI:10.1177/002199838301700307

26. Obradovic J., Boria S., Belingardi G. Lightweight design and crash analysis of composite frontal impact energy absorbing structures. Composite Structures. 2012; 94(2): 423–430. Available at: DOI:10.1016/j.compstruct.2011.08.005

27. Sun G., Li S., Liu Q., Li G., Li Q. Experimental study on crashworthiness of empty / aluminum foam / honeycomb-filled CFRP tubes. Composite Structures. Elsevier Ltd; 2016; 152: 969–993. Available at: DOI:10.1016/j.compstruct.2016.06.019

28. Rabiee A., Ghasemnejad H. Effect of multi stitched locations on high speed crushing of composite tubular structures. Composites Part B: Engineering. 2016; 100: 164–175. Available at: DOI:10.1016/j.compositesb.2016.06.068

29. Czaplicki MJ., Robertson RE., Thornton PH. Comparison of bevel and tulip triggered pultruded tubes for energy absorption. Composites Science and Technology. 1991; 40(1): 31–46. Available at: DOI:10.1016/0266-3538(91)90041-M

30. Palanivelu S., Van Paepegem W., Degrieck J., Van Ackeren J., Kakogiannis D., Van Hemelrijck D., et al. Experimental study on the axial crushing behaviour of pultruded composite tubes. Polymer Testing. 2009; 29(2): 224–234. Available at: DOI:10.1016/j.polymertesting.2009.11.005

31. Huang J., Wang X. On a new crush trigger for energy absorption of composite tubes. International Journal of Crashworthiness. 2010; 15(6): 625–634. Available at: DOI:10.1080/13588265.2010.484194

32. Huang JC., Wang XW. Effect of the SMA trigger on the energy absorption characteristics of CFRP circular tubes. Journal of Composite Materials. 2010; 44(5): 639–651. Available at: DOI:10.1177/0021998309347572

33. Jiménez MA., Miravete A., Larrodé E., Revuelta D. Effect of trigger geometry on energy absorption in composite profiles. Composite Structures. 2000; 48(1): 107–111. Available at: DOI:10.1016/S0263-8223(99)00081-1

34. Tong Y., Xu Y., Wang J., Suman B. Energy absorption capability of carbon fiber reinforced plastic tubes with semi-circle grooved external trigger. Journal of Reinforced Plastics and Composites. 2016; 35(20): 1460–1476. Available at: DOI:10.1177/0731684416654579

35. Zhang Z., Sun W., Zhao Y., Hou S. Crashworthiness of different composite tubes by experiments and simulations. Composites Part B. Elsevier; 2018; 143(June 2016): 86–95. Available at: DOI:10.1016/j.compositesb.2018.01.021

36. Palanivelu S., Van Paepegem W., Degrieck J., Kakogiannis D., Van Ackeren J., Van Hemelrijck D., et al. Comparative study of the quasi-static energy absorption of small-scale composite tubes with different geometrical shapes for use in sacrificial cladding structures. Composite Structure. Elsevier Ltd; 2010; 29(0): 1–22. Available at: DOI:10.1016/j.polymertesting.2010.01.003

37. Yan T., Wang J. Crashworthy component design of an ultra-light helicopter with energy absorbing composite structure. Procedia Engineering. 2014; 80: 329–342. Available at: DOI:10.1016/j.proeng.2014.09.091

38. Ghasemnejad H., Hadavinia H., Aboutorabi A. Effect of delamination failure in crashworthiness analysis of hybrid composite box structures. Materials and Design. 2010; 31(3): 1105–1116. Available at: DOI:10.1016/j.matdes.2009.09.043

39. Ghasemnejad H., Blackman BRK., Hadavinia H., Sudall B. Experimental studies on fracture characterisation and energy absorption of GFRP composite box structures. Composite Structures. 2008; 88(2): 253–261. Available at: DOI:10.1016/j.compstruct.2008.04.006

40. Warrior NA., Turner TA., Robitaille F., Rudd CD. The effect of interlaminar toughening strategies on the energy absorption of composite tubes. Composites Part A: Applied Science and Manufacturing. 2004; 35(4): 431–437. Available at: DOI:10.1016/j.compositesa.2003.11.001

41. Lavoie JA., Kellas S. Dynamic crush tests of energy-absorbing laminated composite plates. Composites Part A: Applied Science and Manufacturing. 1996; 27(6): 467–475. Available at: DOI:10.1016/1359-835X(95)00058-A

42. Bin Mohamed Rehan MS., Rousseau J., Fontaine S., Gong XJ. Experimental study of the influence of ply orientation on DCB mode-I delamination behavior by using multidirectional fully isotropic carbon/epoxy laminates. Composite Structures. Elsevier Ltd; 2017; 161: 1–7. Available at: DOI:10.1016/j.compstruct.2016.11.036

43. Tao J., Sun CT. Influence of ply orientation on delamination in composite laminates. Journal of Composite Materials. 1998. pp. 1933–1947. Available at: DOI:10.1177/002199839803202103

44. Hussain NN., Prakash S., Daseswara Y V. Comparative Study of Trigger Configuration for Enhancement of Crashworthiness of Automobile Crash Box Subjected to Axial. Procedia Engineering. The Author(s); 2017; 173: 1390–1398. Available at: DOI:10.1016/j.proeng.2016.12.198

45. Chatla P. LS-Dyna for Crashworthiness of Composite Structures. University of Cincinnati; 2012.

46. SHD Composite Materials Ltd. SHD Composites. 2018. Available at: http://shdcomposites.com/ (Accessed: 4 July 2018)

47. SHD Composites. MTC510 UD300 T700 Epoxy Component Prepreg Mechanical Data. [Datasheet]. 2018.

48. Livermore Software Technology Corporation. LS-PrePost Online Documentation. 2012. Available at: http://www.lstc.com/lspp/ (Accessed: 19 July 2018)

49. Livermore Software Technology Corporation. LS-DYNA R9.0 Keyword User's Manual Volume I. 2016.

50. Livermore Software Technology Corporation. LS-DYNA R9.0 Keyword User's Manual Volume II - Material Models. 2016.

51. Livermore Software Technology Corporation. LS-DYNA R9.0 Keyword User's Manual Volume III - Multi-Physics Solvers. 2016.

52. Rabiee A., Ghasemnejad H. Laminate Tailoring of Composite Tubular Structures to Improve Crashworthiness Design at Off-Axis Loading. Open Journal of Composite Materials. 2018; 08(03): 84–109. Available at: DOI:10.4236/ojcm.2018.83008

53. Schön J. Coefficient of friction of composite delamination surfaces. Wear. 2000; 237(1): 77–89. Available at: DOI:10.1016/S0043-1648(99)00315-4